Stem Cell Reports
Article

ISSCR

OPEN ACCESS

Gene expression dynamics underlying cell fate emergence in 2D micropatterned human embryonic stem cell gastruloids

Kyaw Thu Minn,[1,2] Sabine Dietmann,[2,5,6] Sarah E. Waye,[2] Samantha A. Morris,[2,3,4] and Lilianna Solnica-Krezel[2,4,*]

[1]Department of Biomedical Engineering, Washington University, St. Louis, MO 63130, USA
[2]Department of Developmental Biology, Washington University School of Medicine, St. Louis, MO 63110, USA
[3]Department of Genetics, Washington University School of Medicine, St. Louis, MO 63110, USA
[4]Center of Regenerative Medicine, Washington University School of Medicine, St. Louis, MO 63110, USA
[5]Division of Nephrology, Washington University School of Medicine, St. Louis, MO 63110, USA
[6]Institute for Informatics, Washington University School of Medicine, St. Louis, MO 63110, USA
*Correspondence: solnical@wustl.edu
https://doi.org/10.1016/j.stemcr.2021.03.031

SUMMARY

Human embryonic stem cells cultured in 2D micropatterns with BMP4 differentiate into a radial arrangement of germ layers and extraembryonic cells. Single-cell transcriptomes demonstrate generation of cell types transcriptionally similar to their *in vivo* counterparts in Carnegie stage 7 human gastrula. Time-course analyses indicate sequential differentiation, where the epiblast arises by 12 h between the prospective ectoderm in the center and the cells initiating differentiation toward extraembryonic fates at the edge. Extraembryonic and mesendoderm precursors arise from the epiblast by 24 h, while nascent mesoderm, endoderm, and primordial germ cell-like cells form by 44 h. Dynamic changes in transcripts encoding signaling components support a BMP, WNT, and Nodal hierarchy underlying germ-layer specification conserved across mammals, and FGF and HIPPO pathways being active throughout differentiation. This work also provides a resource for mining genes and pathways expressed in a stereotyped 2D gastruloid model, common with other species or unique to human gastrulation.

INTRODUCTION

Early mammalian embryogenesis entails sequential specification of extraembryonic (ExE) and embryonic tissues, from which the three germ layers, ectoderm, mesoderm, and endoderm, arise and are shaped into the body plan during gastrulation (Shahbazi and Zernicka-Goetz, 2018). The underlying cellular and molecular mechanisms have been extensively investigated in the mouse and, more recently, in nonhuman primates, *in vitro* cultured human embryos, and 2D or 3D human embryonic stem cell (hESC) models (Ghimire et al., 2021).

Prior to implantation, the totipotent zygote gives rise to a blastocyst consisting of an inner cell mass (ICM), trophectoderm (TE), and primitive endoderm (PE or hypoblast). While preimplantation lineage segregation processes are generally conserved between mouse and human, differences in timing and molecular mechanisms emerge (Molè et al., 2020). In early human and monkey embryos, blastocyst cells co-express lineage-specific genes, with concurrent establishment of TE, mature hypoblast, and ICM not observed until implantation (Nakamura et al., 2016; Petropoulos et al., 2016; Xiang et al., 2019). After implantation in humans, the ICM forms an epiblast (EPI) and amniotic epithelium surrounding the amniotic cavity. The latter develops later in the mouse and via different mechanisms (Molè et al., 2020). Moreover, post-implantation EPI in humans is shaped like a flat disk, but like a cup in mouse.

Gastrulation starts with the formation of the primitive streak (PS) in the posterior side of the EPI disk. In mouse, ExE cells surrounding the EPI secrete Bmp4, which in turn induces the Wnt3 and Nodal signaling cascade in the EPI (Ben-Haim et al., 2006). WNT and NODAL activities are restricted to the posterior EPI by Lefty1, Cer1, and Dkk1 inhibitors secreted from the anterior visceral endoderm, establishing the anterior-posterior axis (Morgani and Hadjantonakis, 2020). At the posterior EPI, high Nodal and Wnt3 signaling induces the expression of T (TBXT or Brachyury), marking mesoderm precursors, which undergo the epithelial-to-mesenchymal transition (EMT), resulting in the PS formation. As the EMT wave extends the PS anteriorly, mesendoderm precursors enter via the PS and migrate to form mesoderm and endoderm, while the remaining EPI becomes ectoderm (Williams et al., 2012). Fgf8 is necessary for cell movement away from the PS in the mouse (Sun et al., 1999), but low *FGF8* expression in Carnegie stage (CS) 7 human gastrula implies that alternative FGF ligands act during human gastrulation (Tyser et al., 2020). Murine *Bmp4* mutants fail to express T or form mesoderm and manifest truncated posterior structures (Mishina et al., 1995). Thus, the interplay of the BMP, WNT, NODAL, and FGF pathways underlies germ layer specification and morphogenesis during mouse gastrulation (Morgani and Hadjantonakis, 2020).

Due to the ease of genetic manipulation and the ability to finely control experimental factors, *in vitro* stem cell

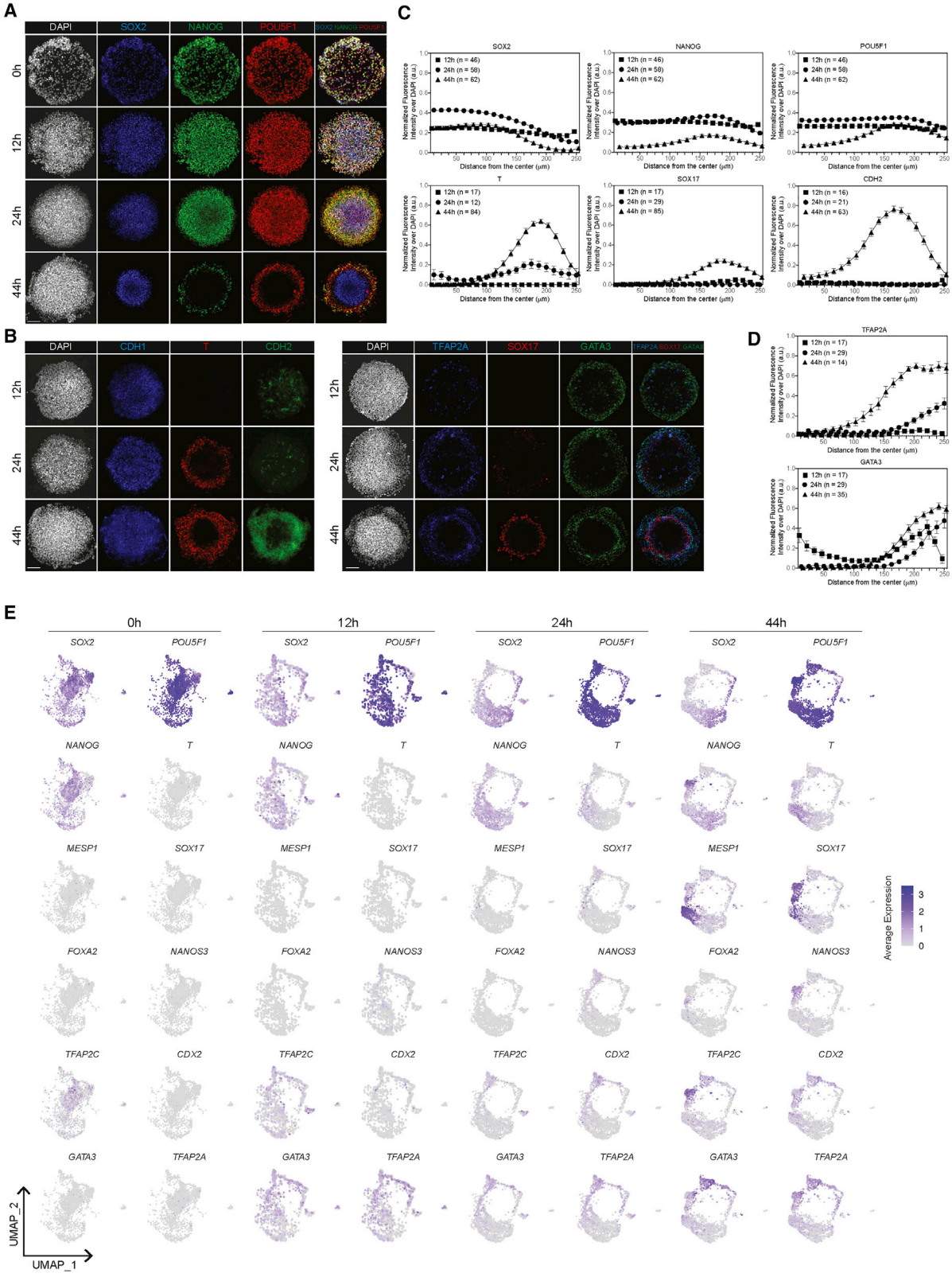

(legend continued on next page)

systems have emerged as an invaluable tool for understanding the signaling cascades and transcriptional regulatory network underlying cell fate specification and morphogenesis during early human development (Ghimire et al., 2021). These models include 2D micropatterned and 3D gastruloid (Martyn et al, 2018, 2019a; Moris et al., 2020; Warmflash et al., 2014), and 3D early blastocyst (Rivron et al., 2018) and pre-gastrulation EPI (Simunovic et al., 2019) models. The 2D and 3D gastruloid gene expression patterns are similar to those of CS7 (Minn et al., 2020) and CS9 human embryos (Moris et al., 2020), respectively. While both 2D and 3D gastruloids differentiate into germ layers, those of the former are highly reproducible and thus suitable for investigating dynamic gene expression changes underlying cell fate emergence during early human gastrulation (Minn et al., 2020; Warmflash et al., 2014).

As in mouse gastrulation, the BMP, WNT, and NODAL pathways interact in hESC 2D micropatterned gastruloids, which form germ layers and ExE cell types upon BMP4 treatment (Chhabra et al., 2019; Etoc et al., 2016; Martyn et al., 2018; Minn et al., 2020; Tewary et al., 2017; Warmflash et al., 2014). In 2D micropatterned gastruloids, despite global BMP4 treatment, BMP signaling is restricted to the edge and activates WNT, which in turn activates NODAL signaling. WNT and NODAL activities then travel from the edge toward the center as indicated by phosphorylation and/or nuclear localization of the downstream effectors SMAD1, SMAD2/3, and CTNNB1 (β-catenin) (Chhabra et al., 2019; Etoc et al., 2016). However, the spatiotemporal transcriptional dynamics of these pathways' components and the transcription factors underlying cell fate emergence in micropatterned gastruloids are incompletely understood.

Using single-cell RNA sequencing (scRNA-seq), we previously reported that BMP4 treatment of hESCs in 2D micropatterns generates ectoderm, EPI-like cells, PS-like cells, nascent mesoderm, endoderm, human primordial germ cell (PGC)-like cells (hPGCLCs), and ExE-like cells with amnion and TE signatures (Minn et al., 2020). Here, we performed a time course of immunofluorescence (IF) and scRNA-seq on micropatterned cultures at 0, 12, 24, and 44 h of BMP4 application. We show that germ layer formation in 2D gastruloids follows the temporal order of *in vivo* gastrulation, with EPI and ectoderm precursors forming by 12 h and mesendoderm precursors emerging by 24 h to give rise to nascent mesoderm and endoderm by 44 h, when hPGCLCs are also present. A comparison with CS7 human gastrula (Tyser et al., 2020) showed similarities in transcriptomes and differentiation trajectories of gastruloid cells to those of their *in vivo* counterparts. Dynamic changes in transcripts encoding signaling components support a BMP, WNT, and NODAL hierarchy underlying germ layer specification conserved across mammals, and FGF and HIPPO signaling being active over the course of differentiation.

RESULTS

H1 hESCs cultured on 500 μm diameter extracellular matrix microdiscs and treated for 44 h with BMP4 in mTeSR, which includes TGF-β and FGF2 ligands, reproducibly recapitulate aspects of gastrulation, namely, the formation of germ layers, and PGC-like and ExE-like cells (Minn et al., 2020; Warmflash et al., 2014). Here, we performed a time-course study of scRNA-seq and IF analyses on these 2D micropatterned cultures at 0 h (just before BMP4 addition) and 12, 24, and 44 h after BMP4 addition (Minn et al., 2020), to investigate cell differentiation trajectories and underlying dynamic gene expression, and deduce cell signaling interactions leading to the formation of these early embryonic cell types. ScRNA-seq datasets for two replicates at each time point were generated from cells pooled from 36 individual colonies per replicate (Figure S1A). In total, 9,167 cells expressing 24,190 genes were analyzed.

Sequential emergence of the seven embryonic and extraembryonic cell types

Two-dimensional micropatterned colonies before BMP4 treatment (0 h) expressed POU5F1, SOX2, and NANOG uniformly (Figures 1A and 1E). At 12 h of BMP4 treatment, high pSMAD1 staining was restricted to the colony edge (Figure S1B), consistent with previous reports (Etoc et al., 2016; Warmflash et al., 2014). TE marker GATA3 expression was generally confined to the outer edge, suggesting the

Figure 1. Temporal dynamics of protein and gene expression along the time course of 2D micropatterned gastruloid BMP4 treatment

(A and B) Immunofluorescence images of (A) SOX2, NANOG, and POU5F1 and (B) CDH1, T, CDH2, TFAP2A, SOX17, and GATA3 at the indicated time points. Scale bar, 100 μm.

(C and D) Quantification of normalized fluorescence intensity of (C) SOX2, NANOG, POU5F1, T, SOX17, and CDH2 and (D) TFAP2A and GATA3 after 12, 24, and 44 h of BMP4 treatment. Number of experiments, n = 1 for T, SOX17, CDH2, GATA3, and TFAP2A at 12 and 24 h; n = 1 for TFAP2A at 44 h; n = 2 for GATA3 at 44 h; n = 3 for SOX2, NANOG, and POU5F1 at 12, 24, and 44 h; n = 5 for T and CDH2 at 44 h; n = 6 for SOX17 at 44 h. Data are presented as the mean ± SEM.

(E) Uniform manifold approximation and projection (UMAP) display of indicated marker expression at indicated time points.

initiation of differentiation (Gunne-Braden et al., 2020). However, the amnion marker TFAP2A was expressed in fewer cells and not as confined to the edge as GATA3 (Figure 1B). Neither the PS and mesoderm marker T nor the endoderm marker SOX17 was detected at this stage (Figures 1B and 1E). A few cells in the center were SOX2^{+} with slightly lower levels of POU5F1 and NANOG, suggestive of a prospective ectoderm identity (Figure 1A). Cells between the GATA3^{+} edge and the SOX2^{+}POU5F1^{low} center were SOX2^{+}POU5F1^{high}NANOG^{high}, indicative of pluripotent or EPI-like characteristics.

At 24 h, SOX2^{+}POU5F1^{low}NANOG ^{low} prospective ectoderm cells were more restricted to the center (Figures 1A and 1C). IF studies showed a ring of T expression but only sporadic SOX17^{+} cells (Figure 1B), as corroborated by scRNA-seq (Figure 1E). In mouse gastrulae, cells in the forming PS undergo EMT, characterized by a CDH1-to-CDH2 switch. At 24 h, EMT marker CDH2 expression was sporadic and not restricted to T^{+} cells, while CDH1 expression was observed throughout the gastruloids. The nascent mesoderm marker *MESP1* was also absent (Figure 1E). We interpret these results to mean that T^{+} mesendoderm precursors have emerged, but the EMT has not been initiated by 24 h. The expression of *CDX2*, *GATA3*, and *TFAP2A* was confined to a distinct cell cluster (Figure 1E), and IF staining indicated these cells were confined to the edge (Figures 1B and 1D).

By 44 h, the full complement of ExE, germ layers, and hPGCLCs had formed. CDH2 was restricted to T^{+} cells in IF, consistent with mesoderm precursors acquiring EMT characteristics (Figure 1B) (Minn et al., 2020). ScRNA-seq distinguished *T*$^{+}$ cells into *T*^{high}*MESP1*^{low} and *T*^{low}*MESP1*^{high}, suggestive of PS-like and nascent mesoderm identity, respectively (Figure 1E). A distinct ring of SOX17 expression suggested endoderm formation. ScRNA-seq distinguished *SOX17*$^{+}$ cells into *SOX17*$^{+}$*FOXA2*$^{+}$ endoderm and *SOX17*$^{+}$*NANOS3*$^{+}$*TFAP2C*$^{+}$ hPGCLCs. Co-expression of SOX17 and TFAP2C in IF corroborated the hPGCLC appearance (Figure S1C). Taken together, these studies suggest that EPI-like, prospective ectoderm, and GATA3^{+} cells that initiate differentiation toward the ExE-like form as early as 12 h. Mesendoderm precursors emerge by 24 h, suggesting the initiation of gastrulation-like events, followed by the formation of mesoderm, endoderm, and hPGCLCs by 44 h.

Using canonical markers and monkey and mouse gastrula datasets (Ma et al., 2019; Pijuan-Sala et al., 2019) as references, we previously annotated seven cell types in 44 h gastruloids: EPI-like, ectoderm, PS-like mesoderm-1, nascent mesoderm-like mesoderm-2, endoderm, hPGCLCs, and ExE-like with amnion and TE signatures (Minn et al., 2020). Here, we combined 0, 12, 24, and 44 h datasets using canonical correlation analysis (CCA) in Seurat (Figure 2A) (Stuart et al., 2019). Most 0 h cells formed a distinct cluster, corroborating that differentiation was initiated by 12 h of BMP4 treatment. We used Seurat to compute predicted cell-type scores for cells at 12 and 24 h using the annotated 44 h dataset as reference. Each 12 and 24 h cell with the highest prediction score for a 44 h cell type was assigned the same cell-type annotation (Figures 2B–2D, S2A, and S2B). The annotation of 12 and 24 h micropatterned cultures largely corroborated marker expression analyses described above. Most 12 h cells were predicted to be EPI-like, but the fraction decreased over time (Figure 2C; 94%, 71%, and 25% at 12, 24, and 44 h, respectively), consistent with the emergence of additional differentiated cell types by 44 h. In line with SOX2^{+}POU5F1^{low}NANOG^{low} marker expression, 5% of 12 h cells were identified as prospective ectoderm and showed upregulated ectoderm markers *VIM*, *NES*, and *ID3* (Figure S2C and Table S1). ExE-like cells were observed at 24 h (9%) and increased in proportion by 44 h (13%) (Figure 2C). At 24 and 44 h, predicted mesoderm-1 cells expressed the PS markers *T* and *MIXL1* (Figures 2E and S2C). By 44 h, the proportion of mesoderm-1 cells was reduced, coincident with the emergence of nascent mesoderm-like mesoderm-2. Likewise, endoderm and hPGCLCs did not appear until 44 h.

Together, the IF and scRNA-seq time-course analyses revealed the differentiation dynamics of germ layers and ExE cell types over 44 h of BMP4 treatment in 2D micropatterned gastruloids: (1) at 0 h, untreated cells expressed pluripotent markers and formed a distinct cluster; (2) EPI-like cells predominated at 12 and 24 h but decreased in proportion by 44 h; (3) precursors of ectoderm and GATA3^{+} cells that initiated differentiation toward the ExE-like fate emerged by 12 h; (4) mesendoderm precursors or mesoderm-1 and ExE-like cells formed by 24 h; and (5) more differentiated cell types, mesoderm-2, endoderm, and hPGCLCs, were primarily observed at 44 h. All annotated clusters expressed corresponding canonical markers (Figures 2E and S2C). The replicates at each time point overlap well, supporting reproducibility of the gene-expression dynamics (Figure S2D).

Comparison of the micropatterned gastruloid cell types with the human Carnegie stage 7 gastrula

We reported that 2D hESC gastruloids treated with BMP4 for 44 h are transcriptionally similar to E7.0–7.5 mouse and 14–16 dpf (days post-fertilization) cynomolgus monkey gastrula (Minn et al., 2020), likely corresponding to CS7 human gastrulae (O'Rahilly and Müller, 1987). Comparison with the recently published scRNA-seq dataset from a single CS7 (~16–19 dpf) human gastrula (Tyser et al., 2020) showed the closest correlation in average gene expression and the highest prediction scores of CS7

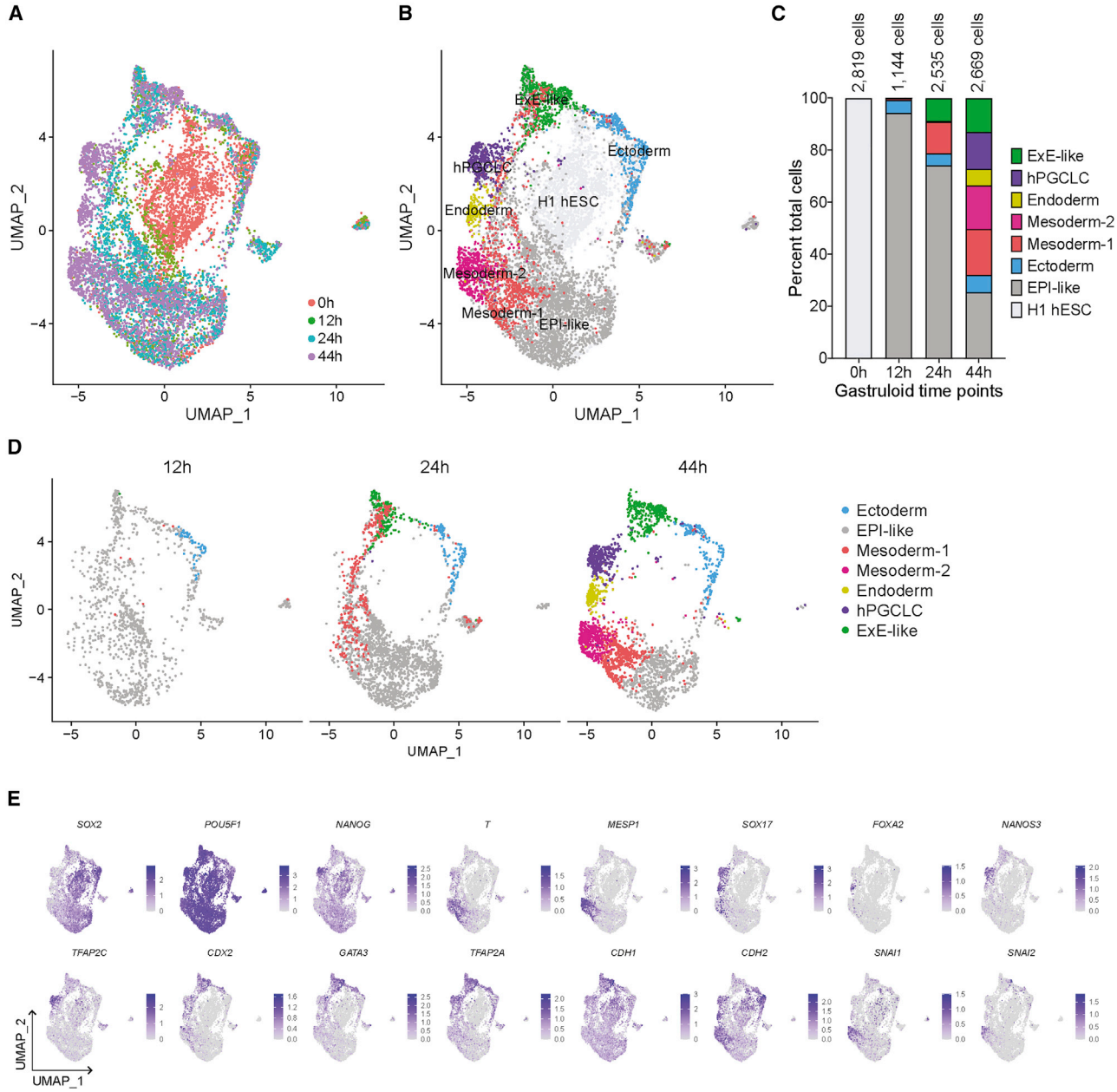

Figure 2. Sequential emergence of the seven embryonic and extraembryonic cell types in micropatterned gastruloids

(A and B) UMAP displays of cells at 0, 12, 24, and 44 h of BMP4 treatment clustered by (A) time and (B) cell type.

(C) Bar plot depicting percentage of cell types at the indicated time points.

(D) UMAPs of the seven cell clusters identified at the indicated time points.

(E) Expression of the indicated markers at 0, 12, 24, and 44 h of BMP4 treatment on the UMAP shown in (B).

human gastrula to 44, 24, 12, and 0 h gastruloids, in that order (Figures 3A and 3B). CS7 human gastrula also transcriptionally corresponds to E7.0–7.5 mouse (Figure S3A) and 14–16 dpf cynomolgus monkey (Figure S3B), similar to 44 h hESC gastruloids (Minn et al., 2020). Thus, 2D hESC gastruloids at 44 h may represent the early to mid-gastrulation stage relevant to CS7 human gastrula.

Transcriptional profiling of the CS7 human gastrula defined 11 major cell types (Figure S3C) (Tyser et al., 2020). Using highly variable genes, we applied Seurat to calculate prediction scores of CS7 gastrula cell types in 2D gastruloids (Figure 3C). Gastruloid EPI-like, mesoderm-1, mesoderm-2, and endoderm scored highly for corresponding CS7 gastrula cell types, namely EPI, PS,

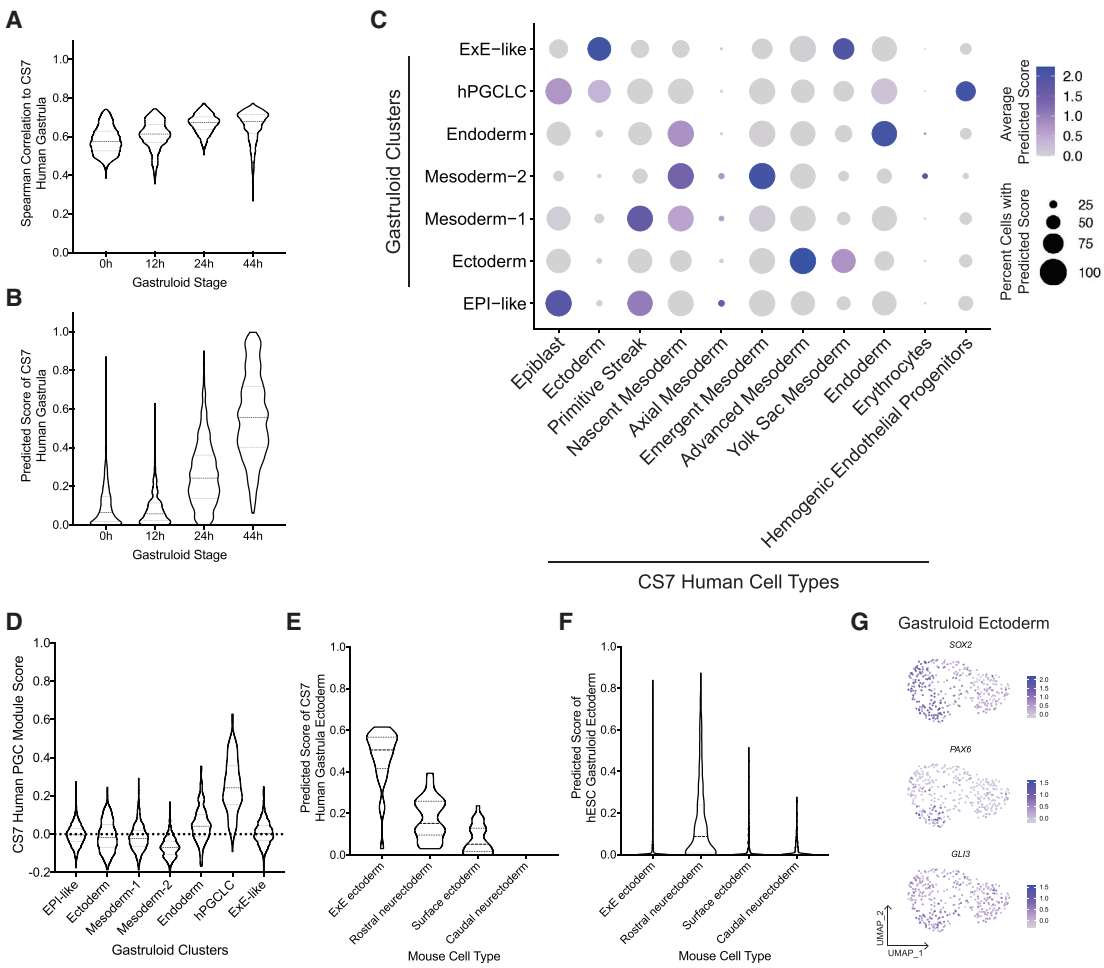

Figure 3. Comparison of the 2D micropatterned gastruloid cell types with the human Carnegie stage 7 gastrula

(A and B) Comparison of CS7 gastrula with BMP4 micropatterned cultures at the indicated time points using (A) average gene expression correlation and (B) anchor-based prediction.

(C) Prediction score of CS7 cell types in the indicated gastruloid cell types.

(D) Violin plot of the PGC module score in gastruloid cell types.

(E and F) Prediction scores of mouse ectodermal derivatives in ectoderm of (E) CS7 and (F) gastruloid.

(G) Expression of indicated ectoderm makers in the gastruloid ectoderm cluster.

nascent/emergent mesoderm, and endoderm, respectively. Within the CS7 PS, seven *NANOS3*$^{+}$*SOX17*$^{+}$*T*^{low} PGCs were identified (Tyser et al., 2020). Similarly, gastruloid hPGCLCs were *NANOS3*$^{+}$*SOX17*$^{+}$*T*^{low} (Figure S2C). The PGC module score using CS7 PGCs' top 20 differentially expressed genes (DEGs) (Tyser et al., 2020) revealed the highest score in the hPGCLC cluster (Figure 3D), indicating that gastruloid hPGCLCs are similar to CS7 PGCs.

In CS7 gastrula, 29 cells (2.4%) were annotated as ectoderm (Tyser et al., 2020), although its embryonic versus ExE identity was unclear, with cells co-expressing the putative primate amnion markers *TFAP2A* and *ISL1* (Yang et al., 2020; Zheng et al., 2019) but lacking the neuroectoderm regulator *SOX2* mRNA (Figure S3D). Thus, CS7 ectoderm cells received high prediction scores for monkey early and late amnion (Figure S3E) and mouse ExE ectoderm (Figure 3E). Correspondingly, we found a high prediction score of gastruloid ExE-like to CS7 ectoderm, monkey amnion and TE derivatives, and mouse ExE ectoderm (Figures S3F). In contrast, gastruloid ectoderm cells had the highest prediction score to mouse rostral neuroectoderm (Figure 3F). *SOX2*, expressed in neuroectoderm derivatives (Pijuan-Sala et al., 2019), was found in gastruloid ectoderm, but not in CS7 ectoderm (Figure S3D). Early neural markers *PAX6* and *GLI3* were also detected in gastruloid ectoderm (Figure 3G).

The comparative transcriptomic analysis with CS7 human gastrula suggests that 2D hESC gastruloids recapitulate the

formation of EPI, PS, nascent/emergent mesoderm, endoderm, and PGC. However, due to the lack of distinct annotation for ectoderm derivatives and ExE TE or amnion in the CS7 dataset, we cannot conclusively determine a similarity of gastruloid ectoderm and ExE-like to their CS7 counterparts. Nonetheless, additional comparisons suggest a transcriptional similarity of gastruloid ectoderm to mouse rostral neuroectoderm (Figure 3F), and gastruloid ExE-like to monkey TE and amnion (Figure S3F).

Dynamic changes in the expression of signaling pathways' components and their transcriptional targets in the course of 2D gastruloid differentiation

Developmental genetic studies defined conserved signaling cascades underlying the induction and patterning of germ layers in all metazoans (Solnica-Krezel, 2020). In post-implantation mouse embryos, Bmp4 ligands from ExE tissues induce in the adjacent EPI expression of Wnt3, which in turn induces expression of Nodal (Morgani and Hadjantonakis, 2020). As previously reported, despite uniform application of BMP4 to 2D micropatterned hESC cultures, its downstream effector pSMAD1 is largely restricted to the edge of each colony after 12 h, and this pattern persists at 24 and 44 h (Figure S1B) (Etoc et al., 2016). Around 24 h, the BMP4 signaling at the edge initiates WNT signaling, which in turn triggers NODAL signaling, and both WNT and NODAL signaling waves travel inward toward the colony center (Chhabra et al., 2019). Consistent with WNT and NODAL activation after 24 h, we found expression of *NODAL*, *WNT3*, and *WNT5A* in the rings of EPI-like and mesoderm-1/2 clusters at 44 h (Figure S4A). We further interrogated our scRNA-seq datasets to understand the expression of components and downstream targets of these and other key signaling pathways and deduce their activity and potential roles in the emergence of the seven gastruloid cell types. Overall, we found increasing expression of BMP, WNT, NODAL, and HIPPO signaling components from 12 to 44 h, while the reverse dynamics were observed for FGF signaling components (Figure 4A).

Within the BMP pathway, the *BMP2* and *BMP7* genes were expressed in the 0 h hESC culture, whereas from 12 to 44 h, we found an increasing expression of genes encoding BMP2 and BMP4 ligands, BMPR2 and BMPR1A receptors, and the SMAD5 downstream effector (Figure 4A). At 44 h, the upregulation of *BMP2* was specific to the mesoderm-2 and endoderm clusters (Figures 4B, S4B, and S4C). Consistent with ExE cells being a source of BMP ligands, the ExE-like cells expressed *BMP4* at levels higher than other cell types (Figure S4A). Over time, the BMP target gene and negative feedback inhibitor, *BAMBI* (Onichtchouk et al., 1999), was also increasingly expressed, particularly in the ExE-like. Among genes encoding BMP antagonists, we saw expression of *NOG* and *FST*, but low *CHRD* across all time points in the ectoderm, and *CER1* in mesoderm-2. Taken together, at 44 h, the strong expression of *FST* in the ectoderm, *CER1* and *BMP2* in mesoderm-2 and endoderm, and *BMP4* in ExE-like is consistent with a radial gradient of BMP signaling activity, with low activity in the center, detected as early as 12 h by IF studies of the downstream effector pSMAD1 (Figure S1B).

WNT signaling is induced by BMP in early mouse embryos and 2D hESC gastruloids (Chhabra et al., 2019). We observed few cells expressing genes encoding WNT ligands during differentiation until 44 h, although receptors *FZD3* and *LRP6*, antagonist *SFRP1/2*, and intercellular components *CTNNB1*, *APC*, and *GS3KB* were broadly expressed (Figures 4A and 4B). At 44 h, we observed expression of WNTs in specific cell populations: *WNT2* in hPGCLC, *WNT3* in mesoderm-1 and -2, *WNT5A* in mesoderm-2, *WNT5B* in hPGCLC and ExE-like, and *WNT6* in ExE-like (Figures 4B and S4D). This suggests that different WNT ligands may be involved in signaling between discrete cell types. Among the WNT antagonists, *SFRP1* was differentially expressed in ectoderm and EPI-like, and *DKK1* in ectoderm and mesoderm-2, whereas *SFRP2* was uniformly expressed in all clusters. Expression of WNT ligands and its target *AXIN2* is indicative of signaling activity. Thus, expression of WNT ligands in all cell types except in the center ectoderm and the surrounding EPI-like ring, particularly at 44 h, suggests low WNT activity in the gastruloid center.

Within the NODAL pathway, starting at 24 h, we saw upregulation in EPI-like and mesoderm-1/2 of *NODAL* and *GDF3* transcripts encoding the ligand heterodimer proposed to induce mesendoderm (Montague and Schier, 2017). Similar expression patterns were observed for *TDGF1* and *FOXH1*, encoding the NODAL co-receptor and transcriptional effector, respectively (Figure 4B). Antagonist *FST* was expressed throughout the time course, and highest in the ectoderm (Figures 4B and S4D). NODAL feedback inhibitors *LEFTY1* and *LEFTY2* were expressed in EPI-like and mesoderm-1 at 24 h, while *LEFTY2* also exhibited enrichment in ectoderm (Figure 4B). These RNA expression data at 24 and 44 h suggest high NODAL signaling activity in the middle ring comprising EPI-like, mesoderm, and endoderm, but low activity in the center ectoderm and ExE-like edge.

Within the FGF pathway, at 0 and 12 h, we noted high RNA expression of ligand FGF2, receptor FGFR1, and antagonists SPRY1, DUSP6, and CBL (Ornitz and Itoh, 2015), which all decreased toward 44 h (Figure 4A). Conversely, we found *FGF17* transcript levels increasing toward 44 h, mainly in mesoderm-1/2 and endoderm (Figures 4B and S4F). *DUSP6*, encoding a negative regulator and target gene, was highly expressed in endoderm (Figure S4F). We also noticed selective upregulation in ectoderm of another

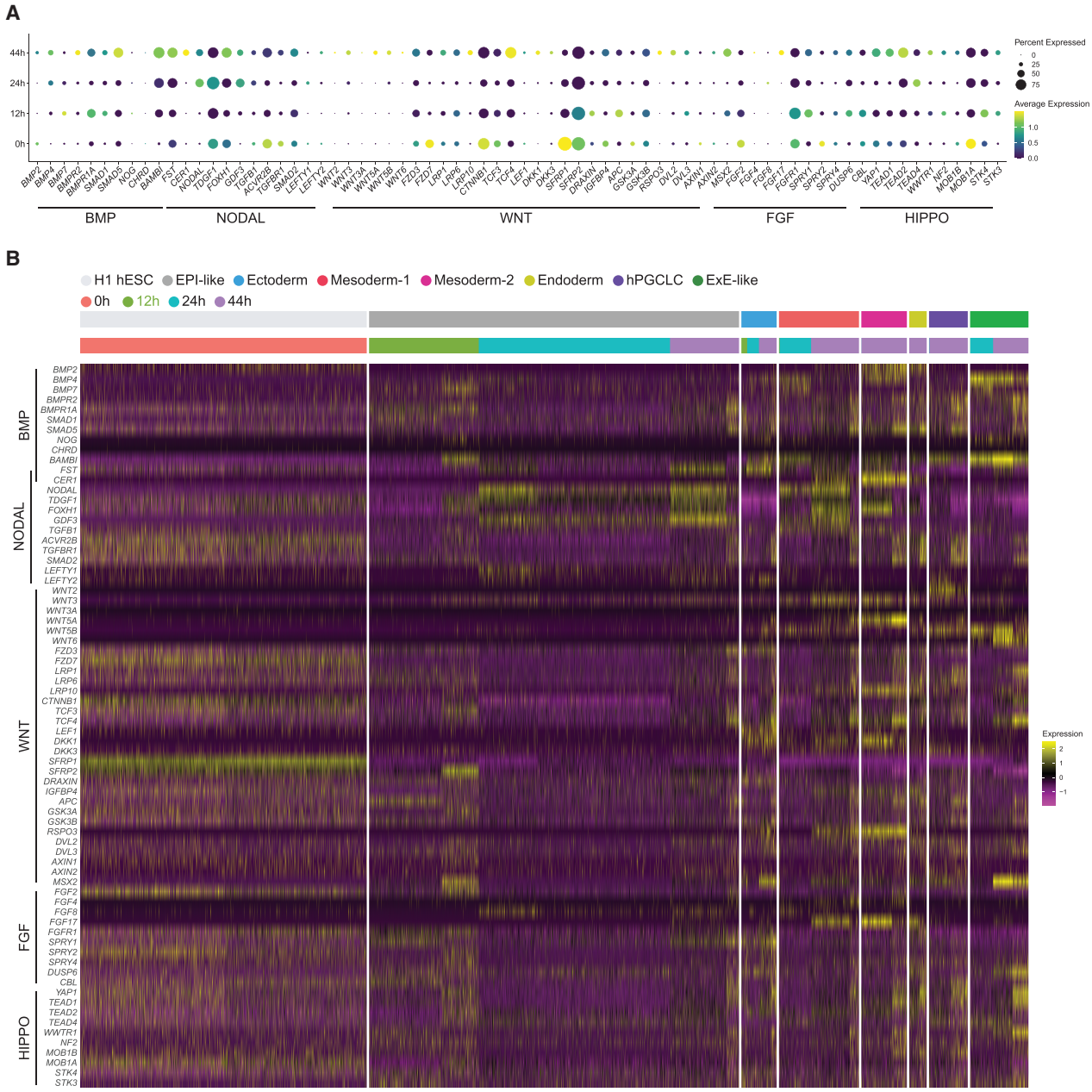

Figure 4. Dynamic changes in the expression of genes encoding signaling pathway components in the course of 2D micropatterned gastruloid differentiation

(A) Temporal gene expression dynamics of the indicated signaling pathway components over the course of BMP4 treatment.

(B) Heatmap showing the expression of components of the indicated pathways in cells for the indicated time points and cell types.

negative regulator, *SPRY1*, suggesting a reduced FGF activity in the center. Cells that produce FGF ligands show the strongest signaling response (Morgani and Hadjantonakis, 2020). Hence, the expression at 44 h of FGF ligands (*FGF2/17*) (Figure 4B), peaking in mesoderm, suggests a circular ring of signaling activity that may play a role in mesoderm and endoderm formation and/or morphogenesis.

Genes encoding HIPPO pathway components were expressed increasingly throughout differentiation, except for the negative regulators *STK4* (*MST1*) and *STK3* (*MST2*), which showed reverse expression dynamics (Figure 4A). Interestingly, we observed high expression in the gastruloid endoderm of *YAP1* and *TEAD1/2* (Figures 4B and S4G), which were also expressed in CS7 definitive

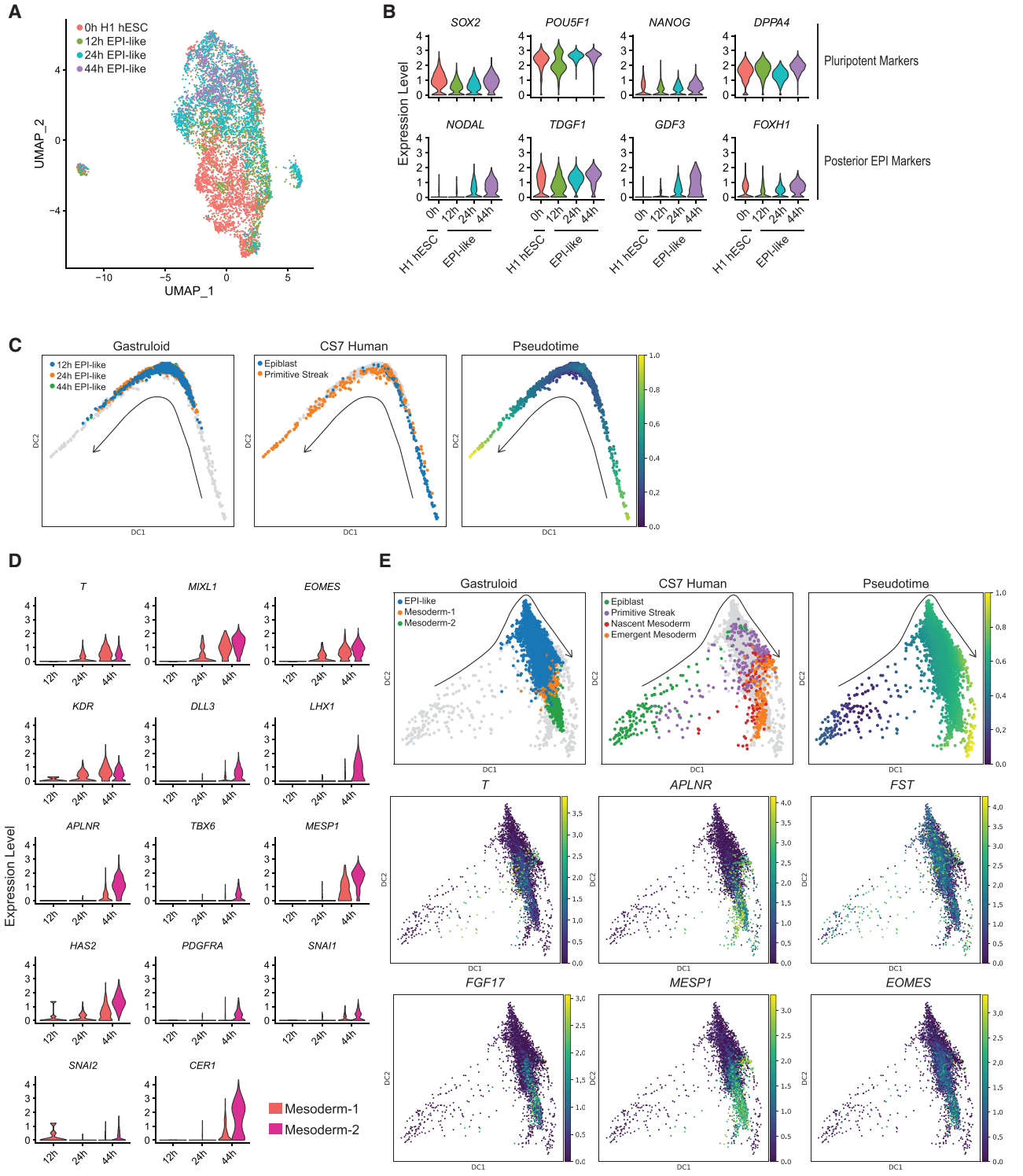

Figure 5. Characterization of gene expression and differentiation trajectory in gastruloid EPI-like and mesoderm clusters

(A) UMAP of untreated cells at 0 h and gastruloid EPI-like cells at 12, 24, and 44 h.

(B) Expression of the indicated markers in the indicated cell types over the gastruloid time course.

(C) Diffusion maps and pseudotime plots of gastruloid EPI-like and CS7 EPI and PS.

(D) Expression of the indicated PS and mesoderm markers in gastruloid mesoderm-1 and -2 clusters over the time course.

(legend continued on next page)

endoderm (DE) (Tyser et al., 2020), implying a potential role for the HIPPO pathway in endoderm formation.

EPI-like cluster represents precursors for gastrulating cells

The gastruloid EPI-like cluster scored highly for EPI in human, monkey, and mouse gastrulae (Figures 3C and S3F). CCA and uniform manifold approximation and projection (UMAP) showed the separation of EPI-like cells from 0 h BMP4-untreated cells (Figure 5A), suggesting an identity distinct from undifferentiated hESCs, but similar to human EPI at gastrulation stages. Toward 44 h, concomitant with the emergence of differentiated cell types, fewer EPI-like cells were identified (Figure 2C). Analyses of untreated 0 h cells and EPI-like cells at 12, 24, and 44 h BMP4 treatment showed expression of the pluripotent markers *SOX2*, *POU5F1*, *NANOG*, and *DPPA4* (Figure 5B). We observed expression of the NODAL pathway's components *TDGF1* and *FOXH1* at 0 h, with increasing expression levels toward 44 h. *GDF3* and *NODAL* expression was appreciably detected only at 24 h and increased by 44 h, suggesting that growing numbers of EPI-like cells at 24 and 44 h are differentiating toward PS-like or mesoderm identity. In support of this, the diffusion map showed an overlap of gastruloid EPI-like along the CS7 EPI-to-PS trajectory (Figure 5C).

Gastruloid mesoderm shows transition of primitive streak to nascent mesoderm identity

Over the course of BMP4 treatment, the majority (>99%) of 12 h (only seven cells) and 24 h mesodermal cells were mesoderm-1, whereas at 44 h, 51% were mesoderm-1 and 49% were mesoderm-2 (Figure S5A), suggesting the progression of mesoderm-1 to mesoderm-2. In CS7, *T* was expressed in PS and nascent mesoderm, but differentiated markers *DLL3*, *MESP1*, *PDGFRA*, and *APLNR*, as well as EMT markers *SNAI1/2*, were expressed only in nascent and emergent mesoderm (Figure S5B). At 24 h, only *T* was expressed in gastruloid mesoderm-1/2, suggestive of PS-like identity. At 44 h, mesoderm-1 expressed relatively higher levels of *T*, but lower levels of differentiated and EMT markers (Figure 5D). These results suggest a shift in gene expression pattern from PS-like to nascent mesoderm by 44 h. Consistent with this, CCA and UMAP of gastruloid mesoderm-1/2 and CS7 PS and mesoderm cell types showed close clustering of mesoderm-1 to PS and mesoderm-2 to nascent/emergent mesoderm (Figure S5C). A diffusion map of CS7 EPI, PS, and nascent/emergent mesoderm showed sequential ordering along the pseudotime and increasing expression of mesoderm markers (Figure 5E). Similar trajectory, pseudotime arrangement, and marker expression dynamics were observed for gastruloid EPI-like, and mesoderm-1 and -2 cells (Figure 5E), suggesting that mesoderm-1 represents a transitional cell type between EPI-like and mesoderm-2, similar to the transitional nature of PS between EPI and nascent mesoderm *in vivo*. Hence, we posit that 2D gastruloid formation recapitulates the temporal aspects of *in vivo* gastrulation, where PS emerges from EPI, and then generates mesoderm and endoderm.

In mouse, Fgf8 is required for the migration of mesodermal cells away from the PS (Sun et al., 1999), yet in primates and hESC gastruloids at 44 h, *FGF8* expression is low or absent in mesoderm (Minn et al., 2020). Instead, *FGF17* is upregulated in gastruloid mesoderm-2 and CS7 nascent mesoderm, implicating different FGF ligands in primate gastrulation (Figures S5D–S5F). *FGF2* was absent in mouse but had high to low expression from EPI to nascent mesoderm transition in human. In gastruloids, we found constant low expression of *FGF2* across EPI-like, mesoderm-1, and mesoderm-2 (Figure S5E). Other notable differences between CS7 human and mouse include upregulation of *SNAI2* but downregulation of *TDGF1* in CS7 EPI to nascent mesoderm transition (Tyser et al., 2020). In mouse, *Snai2* exhibits low expression, whereas *Tdgf1* is upregulated from EPI to nascent mesoderm transition. Similar to CS7 human, we found upregulation of *SNAI2* and slight downregulation of *TDGF1* in gastruloid EPI-like to mesoderm-2 transition (Figures S5D–S5F). To probe further similarities and differences in gene expression changes from EPI to nascent mesoderm (EPI-like to mesoderm-2 in gastruloids), we compared upregulated and downregulated DEGs in mouse, human, and gastruloids. We found more shared DEGs between CS7 and hESC gastruloids compared with mouse (Figure S5G; 158 versus 57 upregulated genes and 95 versus 74 downregulated genes). We also found 22 upregulated and 18 downregulated genes common in all datasets (Figure S5H), including known mesodermal markers *T*, *MESP1*, *SNAI1*, and *MIXL1*. We further identified 136 upregulated and 77 downregulated genes that are shared in CS7 and hESC gastruloids but not in mouse (Figure S5I), arguing that 2D hESC gastruloids can replicate human-specific transcriptional signature of gastrulation.

(E) Diffusion maps showing the arrangements of gastruloid EPI-like and mesoderm-1/2, and CS7 EPI, PS, and nascent/emergent mesoderm. (Top left) Gastruloid cells shown with CS7 cells in the background, (top center) CS7 cells shown with gastruloid cells in the background, and (top right) a pseudotime plot of both gastruloid and CS7 cells combined. (Bottom) Expression of the indicated posterior EPI and mesoderm markers in gastruloid and CS7 cells along the EPI-to-mesoderm transition.

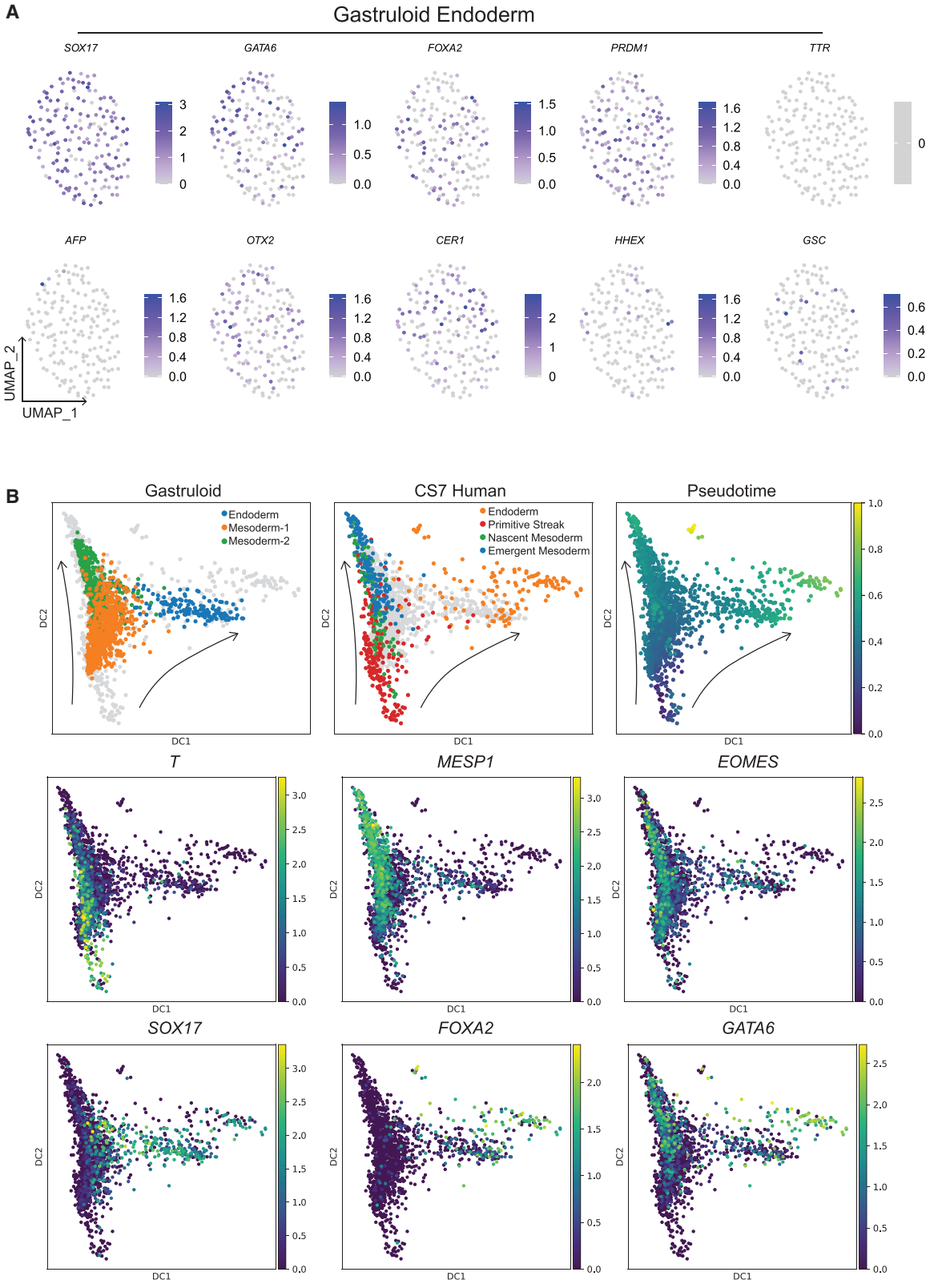

(legend on next page)

Gastruloid endoderm exhibits similar transcriptional signature to definitive endoderm

IF and scRNA-seq data indicated that the endoderm population emerged by 44 h (Figures 1B and 2D). CS7 endoderm can be discerned into DE and PE, based on *TTR* and *AFP* expression in PE (Figures S6A and S6B). Similarly, mouse ExE endoderm expressed *TTR* and *AFP* at higher levels than DE (Figure S6C). In contrast, other endoderm markers, *SOX17*, *GATA6*, and *FOXA2*, were expressed in all CS7 and mouse endoderm. Comparison of CS7 endoderm with E7–7.5 mouse endoderm showed the strongest gene expression correlation between respective definitive and ExE endoderm of human and mouse (Figure S6D), suggesting similar transcriptional signatures between human and mouse endoderm derivatives.

Gastruloid endoderm lacked *TTR* and *AFP* expression, but expressed *SOX17*, *GATA6*, and *FOXA2*, supporting a DE-like identity. Anterior PS markers *OTX2*, *CER1*, *HHEX*, and *GSC*, expressed exclusively in CS7 DE (Tyser et al., 2020), were also found in gastruloid endoderm (Figure 6A). Consistently, we found the highest gene expression correlation of gastruloid endoderm to DE of both mouse and human (Figure S6E). A diffusion map of CS7 PS, nascent/emergent mesoderm, and endoderm showed a bifurcating trajectory from PS to mesoderm or endoderm (Figure 6B). Similar trajectory, pseudotime arrangement, and marker expression were observed for gastruloid mesoderm-1 and -2 and endoderm (Figure 6B). Hence, these results support the notion that gastruloid endoderm models PS-derived DE. Given that gastruloid mesoderm-2 and endoderm appear to arise from mesoderm-1, we posit that mesoderm-1 corresponds to mesendodermal precursors.

Characterization of gastruloid ExE-like cells

ExE markers GATA3 and TFAP2A were detected by IF and scRNA-seq as early as 12 h (Figures 1A and 1E). However, ExE-like cells were identified only at 24 and 44 h (Figures 2C and 2D). Thus, BMP4 treatment induced GATA3 expression by 12 h in the outermost cells, which were also positive for pSMAD1 (Figure S1B) and later differentiated into ExE-like cells, consistent with GATA3 mediating BMP4-induced differentiation in hESC (Gunne-Braden et al., 2020). We combined TE and amnion datasets from *in vitro* monkey (Ma et al., 2019) and pre-gastrulation human embryos (Xiang et al., 2019) to determine specific markers for both cell types (Figure 7A). The combined amnion cluster expressed *CDX2*, *NANOG*, *POU5F1*, *BMP4*, *ISL1*, and *CXCL12*, but TE expressed *KRT7* and *GATA3* (Figure 7C). However, both TE and amnion markers were expressed across all gastruloid ExE-like cells (Figures 7B and 7D). Among DEGs of the combined amnion and TE cluster identified in an unbiased manner, we found 41 TE markers and 54 amnion markers upregulated in the gastruloid ExE-like (Figure S7A). Some markers were expressed at 24 h, and increased toward 44 h, suggesting a progression of ExE-like formation along the time course. Likewise, the prediction score for monkey late amnion-2 and TE increased from 12 to 44 h (Figure S7B). Overall, we interpret these results to mean that gastruloids form an ExE cell type with both amnion and TE signatures, consistent with our analyses at 44 h (Minn et al., 2020), and that both signatures increase over time.

Gastruloid hPGCLCs have transcriptional signatures of gastrulating and amnion cells

In gastruloids, hPGCLCs arise by 44 h of BMP4 treatment, evidenced by *SOX17*, *NANOS3*, and *TFAP2C* co-expression (Figure 2B). These cells exhibited transcriptional signatures similar to those of CS7 and monkey PGCs (Figures S7C–S7E). Over time, in gastruloid hPGCLCs, expression of amnion markers *TFAP2A* and *CDX2,* and gastrulating markers *T* and *MIXL1* increased, but that of TE markers *GATA3* and *KRT7* decreased (Figure S7E). Thus, gastruloid hPGCLCs exhibit gastrulating and amnion transcriptional signatures, as reported for hPGCLCs derived from hESCs in 3D aggregates (Chen et al., 2019). Likewise, we found expression of the gastrulation marker *T* and ExE markers *TFAP2A*, *GATA3*, and *CDX2* in monkey PGCs (Figure S7C). However, in CS7 PGCs, only the gastrulation and no amnion signature was observed (Figure S7D). In monkey, PGCs arise in the amnion, with high BMP and WNT signaling, suggesting their underlying role in PGC specification. In 2D micropatterned gastruloids, *BMP4* was highly expressed in the ExE-like population, whereas its receptors *BMPR1A* and *BMPR2*, as well as target genes *SMAD1* and *SMAD5*, were expressed in hPGCLCs, supporting a potential role of BMP4 signaling from ExE-like populations to hPGCLCs (Figure S4B). Furthermore, complementary expression of WNT ligands (*WNT6* and *WNT5B*) in the ExE-like and receptors (*FZD3* and *LRP1/6*) along with expression of *WNT*2 and *WNT5B* in hPGCLCs points to WNT signaling having a role in gastruloid hPGCLC specification (Figure 4C).

Figure 6. Characterization of gene expression and differentiation trajectory in gastruloid endoderm

(A) Expression of endoderm and anterior PS markers.

(B) Diffusion maps showing arrangements of gastruloid mesoderm-1/2 and endoderm, and CS7 PS, nascent/emergent mesoderm, and endoderm. (Top left) Gastruloid cells shown with CS7 cells in the background, (top center) CS7 cells shown with gastruloid cells in the background, and (top right) a pseudotime plot of both gastruloid and CS7 cells combined. (Bottom) Expression of the indicated mesoderm and endoderm markers in gastruloid and CS7 cells along PS-to-mesoderm and PS-to-endoderm trajectories.

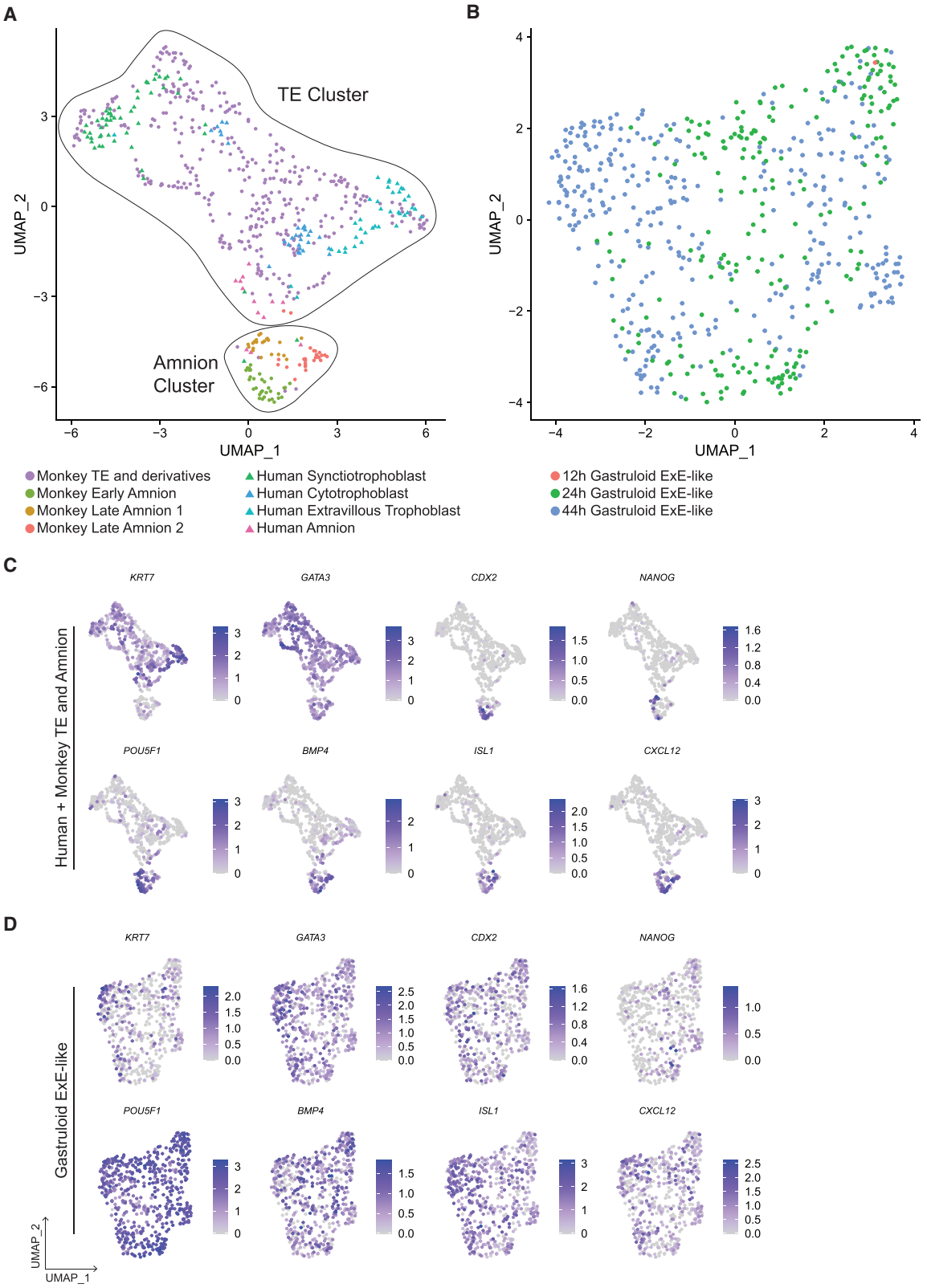

Figure 7. Transcriptional characterization of gastruloid ExE-like cells

(A and B) UMAPs of (A) *in vitro* D6–14 human and 11–17 dpf monkey TE and amnion and (B) gastruloid ExE-like cells.

(C and D) Expression of the indicated markers in (C) human and monkey TE and amnion and (D) gastruloid ExE-like cells.

DISCUSSION

In vitro hESC models have been recently used to study aspects of human gastrulation, including specification of germ layers, organizer, and morphogenetic processes such as the EMT and tissue elongation (Martyn et al, 2018, 2019b; Moris et al., 2020; Simunovic et al., 2019; Warmflash et al., 2014). Using scRNA-seq, we previously demonstrated that 44 h BMP4 treatment of hESCs cultured on a 2D micropattern induces formation of prospective ectoderm, two types of mesoderm, endoderm, EPI-like cells, ExE-like cells, and hPGCLCs (Minn et al., 2020).

The recently available scRNA-seq dataset of one CS7 human gastrula (Tyser et al., 2020) enabled interrogating the 2D hESC gastruloid model. Cross-comparison with CS7 human, mouse (Pijuan-Sala et al., 2019), and monkey (Ma et al., 2019) gastrulae showed that the global transcriptome of hESC gastruloids at 44 h BMP4 treatment resembles that of CS7, E6.0–6.5 mouse, and 14–16 dpf monkey (Figures 3 and S3) (Minn et al., 2020), consistent with the 2D hESC gastruloid modeling aspects of early to mid-gastrulation. Further comparison with CS7 cell types indicated that 2D hESC gastruloids form cell types that are transcriptionally similar to EPI, PS, nascent/emergent mesoderm, DE, and PGC (Figure 3). However, gastruloid prospective ectoderm is not transcriptionally similar to CS7 ectoderm, possibly due to the latter comprising surface and ExE ectoderm (Tyser et al., 2020). Rather, gastruloid ectoderm is transcriptionally similar to mouse rostral neuroectoderm, and expresses markers of nascent neural tissues such as *SOX2*, *GLI3*, and *PAX6* (Pijuan-Sala et al., 2019).

The outermost gastruloid cells have ExE identity as indicated by transcriptional similarity with *in vitro*-cultured D12 and D14 human (Xiang et al., 2019) and 11–17 dpf monkey amnion and TE (Ma et al., 2019). However, distinct amnion or TE identities could not be discerned in gastruloids based on marker gene expression at 44 (Minn et al., 2020) and 24 h time points (this study). Accordingly, a separate study proposed that BMP-treated hESCs are transcriptionally more similar to amnion than TE in the cynomolgus monkey (Chhabra and Warmflash, 2021). These observations are consistent with naive hESCs having a higher potential than primed hESCs to differentiate into ExE lineages and directly give rise to PE (Linneberg-Agerholm et al., 2019) or trophoblast stem cells (Dong et al., 2020).

The emergence of cellular complexity in BMP4-induced 2D gastruloid resembles CS7 human gastrula

Here, we characterized spatiotemporal changes in gene expression over the course of 0,12, 24, and 44 h of BMP4 treatment in 2D micropatterned gastruloids. Our analyses indicate a successive emergence of cell fates, with EPI-like cells, prospective ectoderm, and GATA3$^+$ cells that initiated differentiation by 12 h after BMP4 application, followed by mesendoderm precursors mesoderm-1 and ExE-like by 24 h, and finally, mesoderm-2, endoderm, and hPGCLCs by 44 h. The early emergence of prospective ectoderm is in line with the earlier chromatin accessibility of ectoderm enhancers compared with that of mesendoderm in mouse gastrulae (Argelaguet et al., 2019). The sequential emergence of EPI-like at 12 h, followed by T^+MESP1^- PS-like mesoderm-1 by 24 h, and T^+MESP1^+ mesoderm-2 and $SOX17^+FOXA2^+$ endoderm by 44 h is consistent with studies in mouse, in which posterior EPI gives rise to PS, where cells undergo EMT, migrate, and differentiate into mesoderm and endoderm (Tam and Behringer, 1997). Moreover, the transition from gastruloid EPI-like to mesoderm-1 to mesoderm-2 follows a similar trajectory from EPI to PS to nascent/emergent mesoderm in CS7 human gastrula (Tyser et al., 2020). Similar bifurcating trajectories from CS7 PS to endoderm and mesoderm were found in gastruloid mesoderm-1 to endoderm and mesoderm-2 (Figures 5C, 5E, and 6B), suggesting that mesoderm-1 corresponds to mesendoderm precursors. Based on these analyses we posit that 2D gastruloids model not only the formation but also the sequential emergence and differentiation trajectories of germ layers and ExE cell types during human gastrulation.

Signaling processes underlying cell fate specification in 2D micropatterned gastruloid

Extensive genetic and embryologic studies in fish, frog, chick, and mouse have identified BMP, FGF, Nodal, and Wnt as key signaling pathways underlying vertebrate gastrulation (Solnica-Krezel, 2020). In post-implantation mouse embryos, Bmp4 from ExE induces Wnt3 in posterior EPI, which in turn activates Nodal and induces expression of T, required for the initiation of gastrulation (Ben-Haim et al., 2006). Bmp, Wnt, and Nodal activities are restricted to the posterior by the key inhibitors Cer1, Lefty1, and Dkk1, secreted by anterior visceral endoderm and EPI. By contrast, BMP4 is uniformly applied in 2D micropatterned gastruloids, yet a similar signaling hierarchy with BMP inducing WNT, and WNT inducing NODAL, has been described (Chhabra et al., 2019; Martyn et al., 2018). Likewise, our scRNA-seq indicates high expression of *BMP4* and the negative regulator target gene *BAMBI* in the edge ExE-like cells, suggestive of signaling activity and a source of BMP ligands, similar to mouse (Lawson et al., 1999) and monkey amnion (Yang et al., 2020). *WNT3* was expressed in mesoderm-1/2 and endoderm, and *NODAL* in mesoderm-1 and EPI-like (Figure 4), suggestive of their signaling activities in the domain between the center and the edge of gastruloids, as previously reported (Chhabra et al., 2019;

Martyn et al., 2018). We further showed comprehensive expression patterns of BMP, WNT, NODAL, FGF, and HIPPO pathway genes over the time course of hESC gastruloid differentiation, paving the way for elucidating additional signaling interactions underlying hESC gastruloid formation.

Previous reports on micropatterned cultures using RUES2 hESCs attributed subcellular receptor localization and antagonist *NOG* expression in the center to a radial BMP4 signaling gradient (Etoc et al., 2016). Consistent with this, we found increasing expression of *NOG* in the center ectoderm over time (Figure 4B). *FST*, encoding both BMP and NODAL antagonist, was also high in the center cells (Figure 4). Similar to 2D gastruloids, in the CS7 gastrula, a few cells express *NOG*, but *FST* expression is prevalent in EPI, PS, and nascent mesoderm (Tyser et al., 2020).

In monkey, *ISL1*$^{+}$ amnion expresses *BMP4*, and loss of amnion results in impaired BMP4 signaling and PS formation (Yang et al., 2020). Similarly, in 2D gastruloids, *ISL1*$^{+}$ ExE-like cells strongly expressed *BMP4*, while the adjacent mesoderm-1 cells expressed *BMPR2* and *BMPR1A* receptor. Strong expression of CER1, which can inhibit BMP, WNT, and NODAL (Piccolo et al., 1999), was observed in CS7 nascent mesoderm and gastruloid mesoderm-2. However, *LEFTY2*, expressed in CS7 nascent/emergent mesoderm and mouse nascent mesoderm to restrict NODAL activity to anterior PS and the organizer region, was expressed in few gastruloid cells. Hence, in gastruloids, some aspects of NODAL regulation may not be fully recapitulated, consistent with the absence of the organizer cells in BMP4-induced 2D gastruloid (Martyn et al., 2018; Minn et al., 2020).

The induction of Wnt3 by Bmp4 in posterior EPI is necessary for the induction of T and gastrulation in mouse (Ben-Haim et al., 2006). In addition, Wnt3a, which has an overlapping expression with Wnt3, is necessary for T expression in mouse (Yamaguchi et al., 1999). Although we saw expression of *WNT3* and its target gene *T* in an overlapping pattern, only a few *WNT3A*-expressing cells were found in gastruloids and CS7 gastrula, suggesting that *WNT3* encodes a predominant ligand inducing *T* expression during human gastrulation. Consistent with WNT activity in gastruloid mesoderm cells, *RSPO3*, encoding an amplifier for WNT/β-catenin signaling (Kazanskaya et al., 2008), was distinctly expressed in gastruloid mesoderm-2. *RSPO3* is also expressed in CS7 nascent mesoderm and mouse mesoderm (Pijuan-Sala et al., 2019; Tyser et al., 2020). CS7 nascent mesoderm and gastruloid mesoderm-2 also share expression of *DKK1*, encoding a WNT antagonist (Glinka et al., 1998), although its expression is not observed in mouse mesoderm. Overall, our results suggest conservation of *WNT3* in inducing T in human and mouse, but also a potential role of *DKK1* in human mesoderm differentiation.

FGF signaling, particularly Fgf8-Fgfr1 interaction, is necessary for mesoderm cell migration in mouse gastrulae (Sun et al., 1999). Whereas *FGFR1* is broadly expressed in both hESC gastruloid and human CS7, very few cells express *FGF8* (Tyser et al., 2020). Rather, nascent mesoderm in CS7 expresses *FGF3/17*, while in gastruloids, *FGF17* was primarily expressed in mesoderm-2, implying different FGF ligands are involved in human gastrulation.

Perspective

Our work extends previous studies on 2D micropatterned gastruloid differentiation by elucidating aspects of *in vivo* gastrulation that gastruloids model, including temporal emergence of cell types and comprehensive gene expression changes over the course of 44 h BMP4 treatment. Although the CS7 human dataset is an invaluable resource for querying conservation of cell types and gene expression in the hESC gastruloid systems, the dataset is based on one embryo (Tyser et al., 2020), highlighting the importance of comparisons with mouse and monkey. Using studies from all three mammals as reference, we present data suggesting that gastruloids recapitulate temporal emergence and differentiation trajectories of germ layers of *in vivo* gastrulation. Our data also support conservation of the BMP4, WNT3, and NODAL signaling hierarchy as underlying germ-layer formation, as well as revealing potential features specific to humans, such as *DKK1*, *CER1*, and *FGF17* in mesoderm development. The datasets generated by our work will inform future functional studies to further elucidate signaling and transcriptional networks underlying hESC gastruloid germ-layer formation and, hence, provide insights into *in vivo* human gastrulation.

EXPERIMENTAL PROCEDURES

Microcontact printing

Polydimethylsiloxane stamps with 66 microcylinders of 500 μm diameter each were fabricated using standard photolithography methods as previously described (Minn et al., 2020).

BMP4 differentiation in 2D micropatterns

H1 hESCs of karyotype 46, XY (WiCell, Madison, WI), routinely cultured in Matrigel-coated plates with mTeSR medium (STEMCELL Technologies, Vancouver, BC, Canada), were differentiated with BMP4 in the micropatterned substrates as previously described (Minn et al., 2020).

Immunofluorescence staining and microscopy

After 12, 24, and 44 h, micropatterned cells were washed with PBS, fixed in 4% paraformaldehyde for 30 min, and rinsed twice with PBS at room temperature. Fixed cells were incubated in the blocking solution (0.1% Triton X and 3% normal donkey serum) for 30 min at room temperature. Primary antibodies diluted in the

blocking solution were incubated at 4°C overnight. Cells were then washed with the washing solution (0.1% Tween 20 in PBS) three times, 15 min each, at room temperature. Afterward, secondary antibodies and DAPI at 4 μg/mL (Invitrogen, Carlsbad, CA) in the blocking solution were added for 1 h at room temperature, after which the cells were washed with the washing solution three times, 15 min each, at room temperature.

Images were acquired on an Olympus IX81 inverted spinning disk confocal microscope with 10× or 20× lenses. z-stack images ~150 μm thick were acquired for samples treated with BMP4 for 44 h, but single 2D images were acquired for 12 and 24 h samples. The z-stack images of 44 h samples were projected into single 2D images before analysis.

IF images were processed and analyzed in Fiji (Schindelin et al., 2012). For fluorescence intensity quantification, each image was converted into binary masks. The Concentric Circles plugin was used to overlay 20 equally spaced concentric circles on each masked image, and average fluorescence intensity was measured along each concentric circle. The fluorescence intensity of each marker at each concentric circle was normalized against that of DAPI from corresponding concentric circles of corresponding images. Last, normalized fluorescence intensity was averaged across multiple colonies per marker and presented.

scRNA-seq and data analysis

Single cell collection and scRNA-seq and data analyses were performed as described previously (Minn et al., 2020) and in more detail in the supplemental information.

Data and code availability

The scRNA-seq datasets described in this article were deposited in the GEO database repository under accession GEO nos. GSE144897 and GSE169074.

SUPPLEMENTAL INFORMATION

Supplemental information can be found online at https://doi.org/10.1016/j.stemcr.2021.03.031.

AUTHOR CONTRIBUTIONS

Conceptualization, K.T.M., S.A.M., and L.S.K.; methodology, K.T.M., S.D., S.E.W., S.A.M., and L.S.K.; validation, K.T.M.; formal analysis, K.T.M., L.S.K., and S.D.; investigation, K.T.M. and S.A.M.; data curation, S.A.M. and S.E.W.; writing – original draft, K.T.M. and L.S.K.; writing – review & editing, K.T.M., S.D., S.A.M., S.E.W., and L.S.K.

ACKNOWLEDGMENTS

We thank Sandra Lam (Washington University School of Medicine in St. Louis) and Steven C. George (University of California in Davis) for their guidance and assistance in fabricating polydimethylsiloxane stamps. We thank Yuheng Fu and Chuner Guo (Washington University School of Medicine in St. Louis) for constructing parts of the data curation libraries. We thank Drs. Blerta Stringa and Florence Marlow for comments on the manuscript. This study was funded by Washington University School of Medicine in St. Louis, and a grant from the Children's Discovery Institute, St. Louis to L.S.K., and a Vallee Scholar Award, an Allen Distinguished Investigator Award (through the Paul G. Allen Frontiers Group), a Sloan Research Fellowship, and a New York Stem Cell Foundation Robertson Investigator award to S.A.M.

Received: October 1, 2020
Revised: March 28, 2021
Accepted: March 29, 2021
Published: April 22, 2021

REFERENCES

Argelaguet, R., Clark, S.J., Mohammed, H., Stapel, L.C., Krueger, C., Kapourani, C.-A., Imaz-Rosshandler, I., Lohoff, T., Xiang, Y., Hanna, C.W., et al. (2019). Multi-omics profiling of mouse gastrulation at single-cell resolution. Nature *576*, 487–491. https://doi.org/10.1038/s41586-019-1825-8.

Ben-Haim, N., Lu, C., Guzman-Ayala, M., Pescatore, L., Mesnard, D., Bischofberger, M., Naef, F., Robertson, E.J.J., and Constam, D.B. (2006). The nodal precursor acting via activin receptors induces mesoderm by maintaining a source of its convertases and BMP4. Dev. Cell *11*, 313–323. https://doi.org/10.1016/j.devcel.2006.07.005.

Chen, D., Sun, N., Hou, L., Kim, R., Faith, J., Aslanyan, M., Tao, Y., Zheng, Y., Fu, J., Liu, W., et al. (2019). Human primordial germ cells are specified from lineage-primed progenitors. Cell Rep. *29*, 4568–4582. https://doi.org/10.1016/j.celrep.2019.11.083.

Chhabra, S., Liu, L., Goh, R., Kong, X., and Warmflash, A. (2019). Dissecting the dynamics of signaling events in the BMP, WNT, and NODAL cascade during self-organized fate patterning in human gastruloids. PLoS Biol. *17*, e3000498. https://doi.org/10.1371/journal.pbio.3000498.

Chhabra, S., and Warmflash, A. (2021). BMP-treated human embryonic stem cells transcriptionally resemble amnion cells in the monkey embryo. bioRxiv https://doi.org/10.1101/2021.01.21.427650.

Dong, C., Beltcheva, M., Gontarz, P., Zhang, B., Popli, P., Fischer, L.A., Khan, S.A., Park, K.M., Yoon, E.J., Xing, X., et al. (2020). Derivation of trophoblast stem cells from naïve human pluripotent stem cells. Elife *9*. https://doi.org/10.7554/eLife.52504.

Etoc, F., Metzger, J., Ruzo, A., Kirst, C., Yoney, A., Ozair, M.Z., Brivanlou, A.H., and Siggia, E.D. (2016). A balance between secreted inhibitors and edge sensing controls gastruloid self-organization. Dev. Cell *39*, 302–315. https://doi.org/10.1016/j.devcel.2016.09.016.

Ghimire, S., Mantziou, V., Moris, N., and Martinez Arias, A. (2021). Human gastrulation: the embryo and its models. Dev. Biol. https://doi.org/10.1016/j.ydbio.2021.01.006.

Glinka, A., Wu, W., Delius, H., Monaghan, A.P., Blumenstock, C., and Niehrs, C. (1998). Dickkopf-1 is a member of a new family of secreted proteins and functions in head induction. Nature *391*, 357–362. https://doi.org/10.1038/34848.

Gunne-Braden, A., Sullivan, A., Gharibi, B., Sheriff, R.S.M., Maity, A., Wang, Y.F., Edwards, A., Jiang, M., Howell, M., Goldstone, R., et al. (2020). GATA3 mediates a Fast, Irreversible commitment to BMP4-driven differentiation in human embryonic stem cells.

Cell Stem Cell *26*, 693–706.e9. https://doi.org/10.1016/j.stem.2020.03.005.

Kazanskaya, O., Ohkawara, B., Heroult, M., Wu, W., Maltry, N., Augustin, H.G., and Niehrs, C. (2008). The Wnt signaling regulator R-spondin 3 promotes angioblast and vascular development. Development *135*, 3655–3664. https://doi.org/10.1242/dev.027284.

Lawson, K.A., Dunn, N.R., Roelen, B.A.J., Zeinstra, L.M., Davis, A.M., Wright, C.V.E., Korving, J.P.W.F.M., and Hogan, B.L.M. (1999). Bmp4 is required for the generation of primordial germ cells in the mouse embryo. Genes Dev. *13*, 424–436. https://doi.org/10.1101/gad.13.4.424.

Linneberg-Agerholm, M., Wong, Y.F., Herrera, J.A.R., Monteiro, R.S., Anderson, K.G.V., and Brickman, J.M. (2019). Naïve human pluripotent stem cells respond to Wnt, Nodal and LIF signalling to produce expandable naïve extra-embryonic endoderm. Dev *146*. https://doi.org/10.1242/dev.180620.

Ma, H., Zhai, J., Wan, H., Jiang, X., Wang, X., Wang, L., Xiang, Y., He, X., Zhao, Z.-A., Zhao, B., et al. (2019). In vitro culture of cynomolgus monkey embryos beyond early gastrulation. Science *366*, eaax7890. https://doi.org/10.1126/science.aax7890.

Martyn, I., Brivanlou, A.H., and Siggia, E.D. (2019a). A wave of WNT signalling balanced by secreted inhibitors controls primitive streak formation in micropattern colonies of human embryonic stem cells. Development *146*, dev.172791. https://doi.org/10.1242/dev.172791.

Martyn, I., Kanno, T.Y., Ruzo, A., Siggia, E.D., and Brivanlou, A.H. (2018). Self-organization of a human organizer by combined Wnt and Nodal signalling. Nature *558*, 132–135. https://doi.org/10.1038/s41586-018-0150-y.

Martyn, I., Siggia, E.D., and Brivanlou, A.H. (2019b). Mapping cell migrations and fates in a gastruloid model to the human primitive streak. Development *146*, dev179564. https://doi.org/10.1242/dev.179564.

Minn, K.T., Fu, Y.C., He, S., Dietmann, S., George, S.C., Anastasio, M.A., Morris, S.A., and Solnica-Krezel, L. (2020). High-resolution transcriptional and morphogenetic profiling of cells from micropatterned human esc gastruloid cultures. Elife *9*, 1–34. https://doi.org/10.7554/eLife.59445.

Mishina, Y., Suzuki, A., Ueno, N., and Behringer, R.R. (1995). Bmpr encodes a type I bone morphogenetic protein receptor that is essential for gastrulation during mouse embryogenesis. Genes Dev. *9*, 3027–3037. https://doi.org/10.1101/gad.9.24.3027.

Molè, M.A., Weberling, A., and Zernicka-Goetz, M. (2020). Comparative Analysis of Human and Mouse Development: From Zygote to Pre-gastrulationCurrent Topics in Developmental Biology (Academic Press Inc), pp. 113–138. https://doi.org/10.1016/bs.ctdb.2019.10.002.

Montague, T.G., and Schier, A.F. (2017). Vg1-nodal heterodimers are the endogenous inducers of mesendoderm. Elife *6*. https://doi.org/10.7554/eLife.28183.

Morgani, S.M., and Hadjantonakis, A.K. (2020). Signaling regulation during gastrulation: insights from mouse embryos and in vitro systems. Curr. Top. Dev. Biol., 391–431. https://doi.org/10.1016/bs.ctdb.2019.11.011.

Moris, N., Anlas, K., van den Brink, S.C., Alemany, A., Schröder, J., Ghimire, S., Balayo, T., van Oudenaarden, A., and Martinez Arias, A. (2020). An in vitro model of early anteroposterior organization during human development. Nature *582*, 410–415. https://doi.org/10.1038/s41586-020-2383-9.

Nakamura, T., Okamoto, I., Sasaki, K., Yabuta, Y., Iwatani, C., Tsuchiya, H., Seita, Y., Nakamura, S., Yamamoto, T., and Saitou, M. (2016). A developmental coordinate of pluripotency among mice, monkeys and humans. Nature *537*, 57–62. https://doi.org/10.1038/nature19096.

O'Rahilly, R., and Müller, F. (1987). Developmental Stages in Human Embryos : Including a Revision of Streeter's "Horizons" and a Survey of the Carnegie Collection (Carnegie Institution of Washington).

Onichtchouk, D., Chen, Y.G., Dosch, R., Gawantka, V., Delius, H., Massagué, J., and Niehrs, C. (1999). Silencing of TGF-β signalling by the pseudoreceptor BAMBI. Nature *401*, 480–485. https://doi.org/10.1038/46794.

Ornitz, D.M., and Itoh, N. (2015). The fibroblast growth factor signaling pathway. Wiley Interdiscip. Rev. Dev. Biol. *4*, 215–266. https://doi.org/10.1002/wdev.176.

Petropoulos, S., Edsga, D., Reinius, B., and Linnarsson, S. (2016). Single-cell RNA-seq reveals lineage and X chromosome dynamics in human preimplantation embryos. Cell *165*, 1–15. https://doi.org/10.1016/j.cell.2016.03.023.

Piccolo, S., Agius, E., Leyns, L., Bhattacharyya, S., Grunz, H., Bouwmeester, T., and De Robertis, E.M. (1999). The head inducer cerberus is a multifunctional antagonist of Nodal, BMP and Wnt signals. Nature *397*, 707–710. https://doi.org/10.1038/17820.

Pijuan-Sala, B., Griffiths, J.A., Guibentif, C., Hiscock, T.W., Jawaid, W., Calero-Nieto, F.J., Mulas, C., Ibarra-Soria, X., Tyser, R.C.V., Ho, D.L.L., et al. (2019). A single-cell molecular map of mouse gastrulation and early organogenesis. Nature *566*, 490–495. https://doi.org/10.1038/s41586-019-0933-9.

Rivron, N.C., Frias-Aldeguer, J., Vrij, E.J., Boisset, J.-C.C., Korving, J., Vivié, J., Truckenmüller, R.K., van Oudenaarden, A., van Blitterswijk, C.A., and Geijsen, N. (2018). Blastocyst-like structures generated solely from stem cells. Nature *557*, 106–111. https://doi.org/10.1038/s41586-018-0051-0.

Schindelin, J., Arganda-Carreras, I., Frise, E., Kaynig, V., Longair, M., Pietzsch, T., Preibisch, S., Rueden, C., Saalfeld, S., Schmid, B., et al. (2012). Fiji: an open-source platform for biological-image analysis. Nat. Methods *9*, 676–682. https://doi.org/10.1038/nmeth.2019.

Shahbazi, M.N., and Zernicka-Goetz, M. (2018). Deconstructing and reconstructing the mouse and human early embryo. Nat. Cell Biol. *20*, 878–887. https://doi.org/10.1038/s41556-018-0144-x.

Simunovic, M., Metzger, J.J., Etoc, F., Yoney, A., Ruzo, A., Martyn, I., Croft, G., You, D.S., Brivanlou, A.H., and Siggia, E.D. (2019). A 3D model of a human epiblast reveals BMP4-driven symmetry breaking. Nat. Cell Biol. *21*, 900–910. https://doi.org/10.1038/s41556-019-0349-7.

L. Solnica-Krezel, ed. Gastrulation: from embryonic pattern to form, *136* (Academic Press), Curr. Top. Dev. Biol.

Stuart, T., Butler, A., Hoffman, P., Hafemeister, C., Papalexi, E., Mauck, W.M., Hao, Y., Stoeckius, M., Smibert, P., and Satija, R. (2019). Comprehensive integration of single-cell data. Cell *177*, 1888–1902.e21. https://doi.org/10.1016/j.cell.2019.05.031.

Sun, X., Meyers, E.N., Lewandoski, M., and Martin, G.R. (1999). Targeted disruption of Fgf8 causes failure of cell migration in the gastrulating mouse embryo. Genes Dev. *13*, 1834–1846.

Tam, P.P.L., and Behringer, R.R. (1997). Mouse gastrulation: the formation of a mammalian body plan. Mech. Dev. *68*, 3–25. https://doi.org/10.1016/S0925-4773(97)00123-8.

Tewary, M., Ostblom, J.E., Prochazka, L., Zulueta-Coarasa, T., Shakiba, N., Fernandez-Gonzalez, R., and Zandstra, P.W. (2017). A stepwise model of reaction-diffusion and positional information governs self-organized human peri-gastrulation-like patterning. Development *144*, 4298–4312. https://doi.org/10.1242/dev.149658.

Tyser, R.C.V., Mahammadov, E., Nakanoh, S., Vallier, L., Scialdone, A., and Srinivas, S. (2020). A spatially resolved single cell atlas of human gastrulation. bioRxiv https://doi.org/10.1101/2020.07.21.213512.

Warmflash, A., Sorre, B., Etoc, F., Siggia, E.D., and Brivanlou, A.H. (2014). A method to recapitulate early embryonic spatial patterning in human embryonic stem cells. Nat. Methods *11*, 847–854. https://doi.org/10.1038/nmeth.3016.

Williams, M., Burdsal, C., Periasamy, A., Lewandoski, M., and Sutherland, A. (2012). Mouse primitive streak forms in situ by initiation of epithelial to mesenchymal transition without migration of a cell population. Dev. Dyn. *241*, 270–283. https://doi.org/10.1002/dvdy.23711.

Xiang, L., Yin, Y., Zheng, Y., Ma, Y., Li, Y., Zhao, Z., Guo, J., Ai, Z., Niu, Y., Duan, K., et al. (2019). A developmental landscape of 3D-cultured human pre-gastrulation embryos. Nature *577*, 537–542. https://doi.org/10.1038/s41586-019-1875-y.

Yamaguchi, T.P., Takada, S., Yoshikawa, Y., Wu, N., and McMahon, A.P. (1999). T (Brachyury) is a direct target of Wnt3a during paraxial mesoderm specification. Genes Dev. *13*, 3185–3190. https://doi.org/10.1101/gad.13.24.3185.

Yang, R., Goedel, A., Kang, Y., Si, C., Chu, C., Zheng, Y., Chen, Z., Gruber, P.J., Xiao, Y., Zhou, C., et al. (2020). Essential amnion signals for primate primitive streak formation resolved by scRNA map. bioRxiv https://doi.org/10.1101/2020.05.28.118703.

Zheng, Y., Xue, X., Shao, Y., Wang, S., Esfahani, S.N., Li, Z., Muncie, J.M., Lakins, J.N., Weaver, V.M., Gumucio, D.L., and Fu, J. (2019). Controlled modelling of human epiblast and amnion development using stem cells. Nature *573*, 421–425. https://doi.org/10.1038/s41586-019-1535-2.

Stem Cell Reports, Volume *16*

Supplemental Information

Gene expression dynamics underlying cell fate emergence in 2D micro-patterned human embryonic stem cell gastruloids

Kyaw Thu Minn, Sabine Dietmann, Sarah E. Waye, Samantha A. Morris, and Lilianna Solnica-Krezel

Supplemental Experimental Procedures

BMP4 differentiation in 2D micropatterns

H1 hESC were differentiated with BMP4 in the micropatterned substrates as previously described (Minn et al., 2020). Briefly, H1 hESC of karyotype 46, XY (WiCell, Madison, WI), routinely cultured in Matrigel-coated plates with mTeSR media (Stemcell Technologies, Vancouver, Canada), were differentiated with BMP4 in the micropatterned substrates as previously described (Minn et al., 2020). Briefly, H1 cells were dissociated with Accutase (Sigma Aldrich, St. Louis, MO) incubation at 37°C and 5% CO_2 for 8 min. Equal volume of RPMI medium 1640 (Life Technologies, Carlsbad, CA) was added, and the cell solution was centrifuged at 300 rcf (relative centrifugal force) for 5min. After the supernatant was removed, cells were diluted with fresh mTeSR, and seeded onto micropatterns at 132,000–263,000 cells/cm^2 in mTeSR with 10 μM Rho-associated kinase inhibitor (ROCKi Y-27632, Millipore Sigma, Burlington, MA). After 2h, the medium was replaced with fresh mTeSR, and cultured for additional 3h. Afterwards (6h after initial cell seeding), the medium was replaced with mTeSR containing 50 ng/mL BMP4 (R&D Systems, Minneapolis, MN) for 12h, 24h, and 44h.

scRNA-seq and data analysis

Single cells collection and scRNA-seq and data analyses were performed as described previously (Minn et al., 2020). Briefly, micropatterned cells after 12h, 24h, and 44h BMP4 treatment were washed with PBS, and dissociated into single cells with Accutase incubation at 37°C and 5% CO_2 for 10 min. Equal volume of RPMI medium was added, and the solution was centrifuged 300 rcf for 5 min. After the supernatant was removed, cells were diluted at 20,000 cells per 200 μL of cold DPBS-/-. Afterwards, 800 μL of cold

methanol was added dropwise to the cell solution, and incubated on ice for 15 min. The final solution was kept at -80°C until use.

10x Chromium Single Cell 3’ Library & Gel Bead Kit v2, Chromium Next GEM Single Cell 3’ GEM, Library & Gel Bead Kit v3.1, Chromium Next GEM Single Cell 3' Kit v3.1, Chromium Next GEM Chip G Single Cell Kit, Single Index Kit T Set A, and Dual Index Kit TT Set A and Chromium i7 Multiplex Kit (10X Genomics, Pleasanton, CA) were used according to the manufacturer’s instructions to prepare single-cell library. Agilent TapeStation (Agilent Scientific Instruments, Santa Clara, CA) was used to quantify cDNA libraries. Sequencing was performed on Illumina HiSeq 2500 and NextSeq500 (Illumina, San Diego, CA).

The Cell Ranger v.2.1.0 pipeline was used to align reads to a custom hg19 genome build including transgenes, and to generate a digital gene expression matrix. Seurat package (v.3.2.0) was used for processing and visualization (Butler et al., 2018; Stuart et al., 2019). Default settings were used unless noted otherwise. For each dataset, cells with outlier number of genes and mitochondrial gene expression were excluded. We normalized and scaled the filtered expression matrix to remove unwanted sources of variation driven by mitochondrial gene expression, the number of detected UMIs, and the cell cycle. For 24h and 44h datasets, we combined replicates at each time point using canonical correlation analysis selecting for 30 dimensions and 3,000 anchor features (highly variable genes). Next, we combined all 12h, 24h, and 44h datasets using the same parameters. Nonlinear dimensionality reduction by UMAP was performed on the first 30 principal components using the implementation by Seurat. With previously annotated 44h cells serving as reference (Minn et al., 2020), we

annotated cells at 12h and 24h using FindTransferAnchors and TransferData functions in Seurat. This anchor-based approach calculated prediction score in each 12h and 24h cell for referenced 44h cell types. Each 12h or 24h cell with the highest prediction score for a particular 44h cell type was annotated as that cell type. DEGs across cell types or time course were identified using FindMarkers or FindAllMarkers functions, with threshold settings of 0.25 log fold-change and 25% detection rate.

For comparison with published dataset, CCA was used as described above for combining gastruloid datasets. Average gene expression correlation was calculated using Spearman correlation on the basis of highly variable genes from reference datasets. Prediction score was calculated using the anchor-based approach described above, after the reference and query datasets were combined with CCA. Module score was calculated using AddModuleScore function in Seurat, which calculates the difference in average gene expression between a set of marker genes of interest and that of randomly selected genes (Tirosh et al., 2016).

Diffusion maps for single cells were calculated based on the normalized and scaled gene expression data matrix using the R Bioconductor *destiny* package (Angerer et al., 2016), with a number of k-nearest neighbors, knn = 40, and a Gaussian kernel width, sigma = 8, slightly lower than the optimal value of sigma estimated by *destiny*. A probabilistic breadth-first search of the k-nearest neighbor graph was performed and the results of this search were converted into a pseudotime.

To identify genes differentially expressed between emergent cell populations (Ectoderm versus 0h hESCs, Table 1S), we used the Seurat FindMarkers function to compare against all other cells types and used Seurat threshold of logFC > 0.1 and p

value < 0.05 to consider as significant differences in expression. In addition, we inspected the localized expression in a scatterplot.

References:

Angerer P, Haghverdi L, Büttner M, Theis FJ, Marr C, Buettner F. 2016. destiny: diffusion maps for large-scale single-cell data in R. *Bioinfor* **32**:1241–1243. doi:10.1093/bioinformatics/btv715

Butler A, Hoffman P, Smibert P, Papalexi E, Satija R. 2018. Integrating single-cell transcriptomic data across different conditions, technologies, and species. *Nat Biotechnol* **36**:411–420. doi:10.1038/nbt.4096

Stuart T, Butler A, Hoffman P, Hafemeister C, Papalexi E, Mauck WM, Hao Y, Stoeckius M, Smibert P, Satija R. 2019. Comprehensive Integration of Single-Cell Data. *Cell* **177**:1888-1902.e21. doi:10.1016/j.cell.2019.05.031

Tirosh I, Izar B, Prakadan SM, Wadsworth MH, Treacy D, Trombetta JJ, Rotem A, Rodman C, Lian C, Murphy G, Fallahi-Sichani M, Dutton-Regester K, Lin JR, Cohen O, Shah P, Lu D, Genshaft AS, Hughes TK, Ziegler CGK, Kazer SW, Gaillard A, Kolb KE, Villani AC, Johannessen CM, Andreev AY, Van Allen EM, Bertagnolli M, Sorger PK, Sullivan RJ, Flaherty KT, Frederick DT, Jané-Valbuena J, Yoon CH, Rozenblatt-Rosen O, Shalek AK, Regev A, Garraway LA. 2016. Dissecting the multicellular ecosystem of metastatic melanoma by single-cell RNA-seq. *Science (80-)* **352**:189–196. doi:10.1126/science.aad0501

Figure 1S

A

Experiment	# colonies per experiment	# of cells after QC	Average genes per cell	Average UMI per cell
0h Replicate 1	36	1,422	3,121	11,549
0h Replicate 2	36	1,397	3,825	17,352
12h Replicate 1	36	766	4,194	23,756
12h Replicate 2	36	378	4,274	19,899
24h Replicate 1	36	947	4,525	30,756
24h Replicate 2	36	1,588	4,011	25,130
44h Replicate 1	36	1,858	4,981	29,609
44h Replicate 2	36	811	3,801	14,612

B

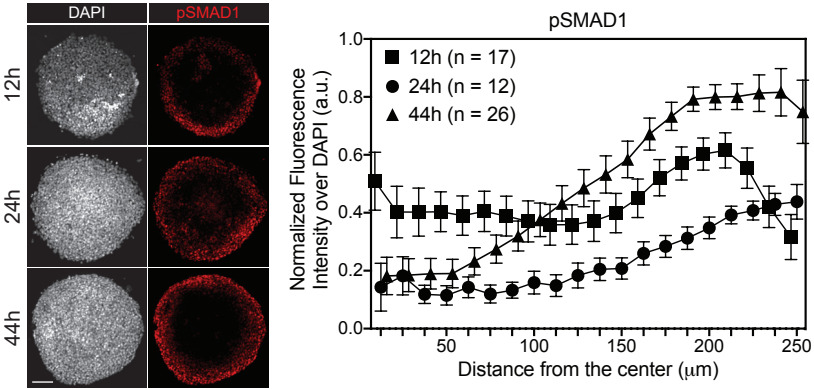

C

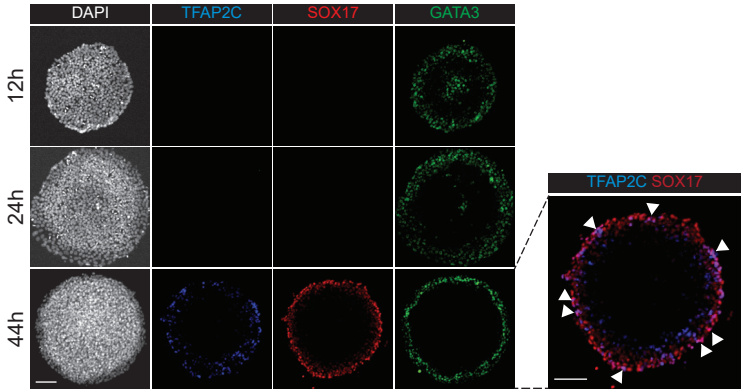

Figure 1S. Supplemental information related to Figure 1

(A) Selected parameters for scRNA-seq analysis.

(B) Immunofluorescence images (left) and quantification of fluorescence intensity (right) for BMP4 downstream effector pSMAD1. Data are represented as mean ± SEM.

(C) Immunofluorescence analysis of SOX17, TFAP2C, and GATA3. Arrow heads indicate selected hPGCLCs co-expressing SOX17 and TFAP2C.

Scale bar is 100μm.

Figure 2S

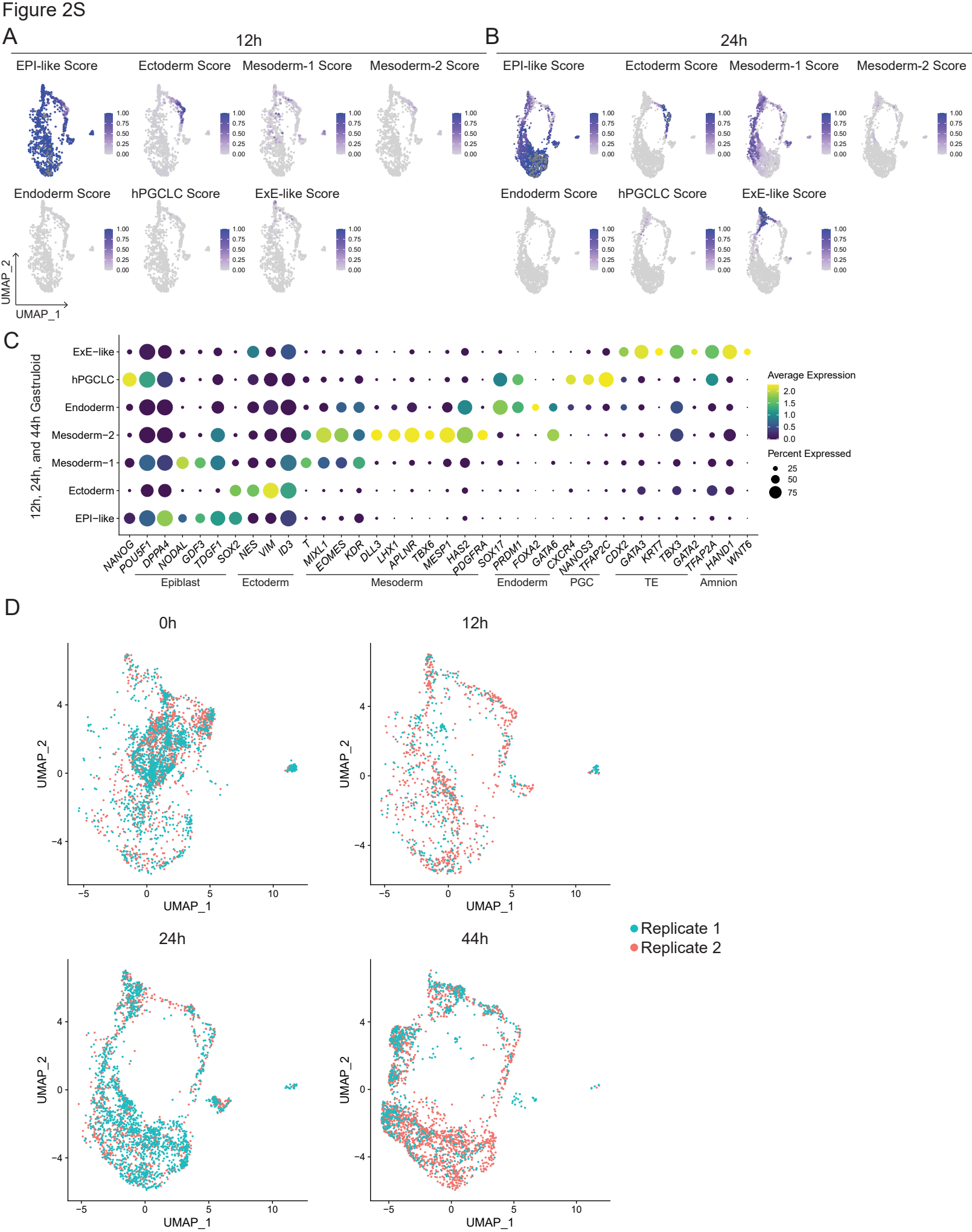
A
12h
B
24h
EPI-like Score
Ectoderm Score
Mesoderm-1 Score
Mesoderm-2 Score
Endoderm Score
hPGCLC Score
ExE-like Score
1.00
0.75
0.50
0.25
0.00
UMAP_2
UMAP_1
C
12h, 24h, and 44h Gastruloid
ExE−like
hPGCLC
Endoderm
Mesoderm−2
Mesoderm−1
Ectoderm
EPI−like
NANOG
POU5F1
DPPA4
NODAL
GDF3
TDGF1
SOX2
NES
VIM
ID3
T
MIXL1
EOMES
KDR
DLL3
LHX1
APLNR
TBX6
MESP1
HAS2
PDGFRA
SOX17
PRDM1
FOXA2
GATA6
CXCR4
NANOS3
TFAP2C
CDX2
GATA3
KRT7
TBX3
GATA2
TFAP2A
HAND1
WNT6
Epiblast
Ectoderm
Mesoderm
Endoderm
PGC
TE
Amnion
Average Expression
2.0
1.5
1.0
0.5
0.0
Percent Expressed
25
50
75
D
0h
12h
24h
44h
UMAP_2
UMAP_1
Replicate 1
Replicate 2

Figure 2S. Supplemental information related to Figure 2

(A and B) Cell type prediction scores for cells treated with BMP4 for 12h (A), and 24h (B), using 44h gastruloid cells as reference.

(C) Dot plots displaying expression of canonical markers of indicated cell types in gastruloid clusters at indicated time points.

(D) UMAP display of overlap between replicates at each indicated time point.

Figure 3S

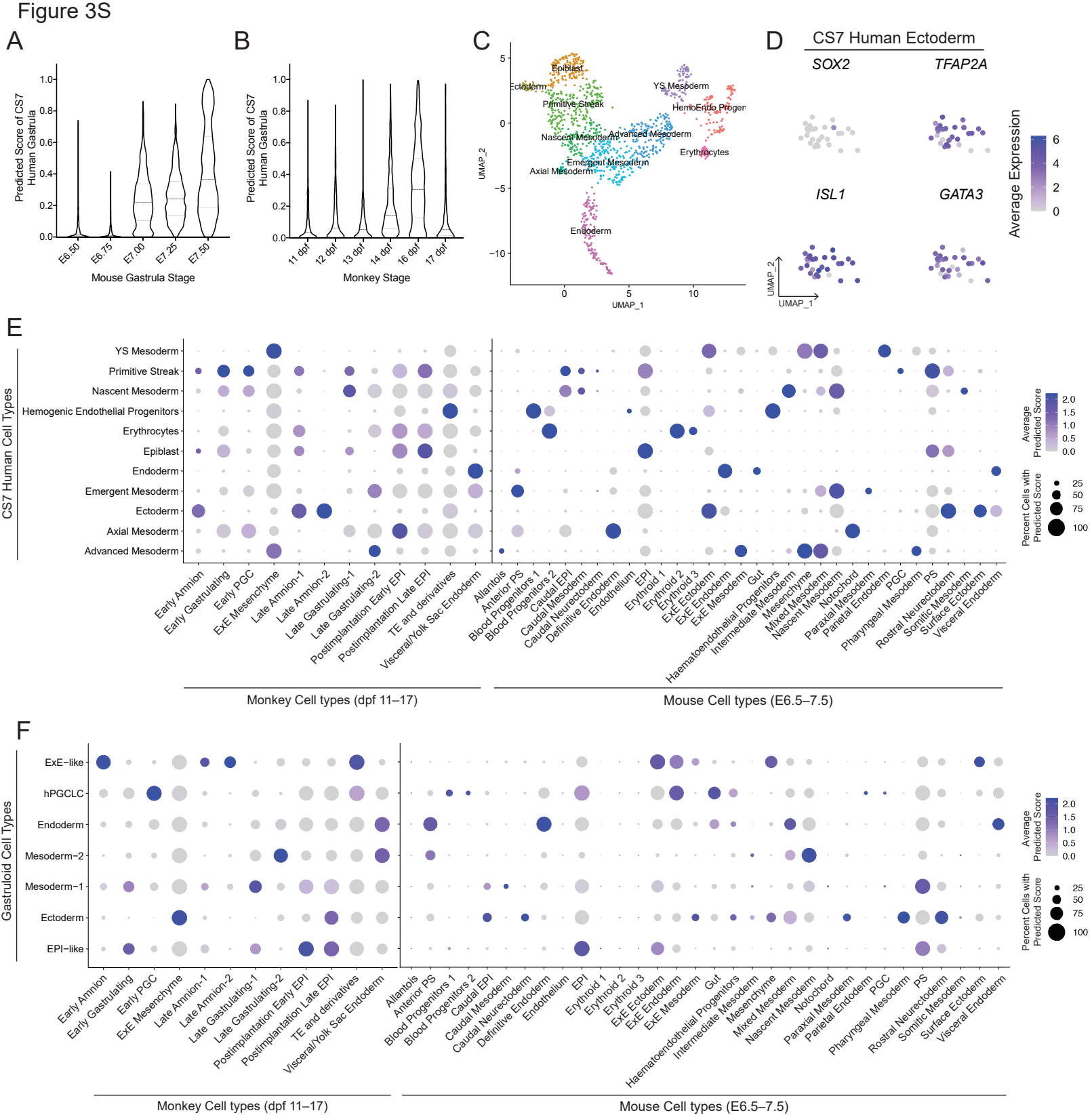
A
Predicted Score of CS7 Human Gastrula
Mouse Gastrula Stage
E6.50
E6.75
E7.00
E7.25
E7.50
B
Predicted Score of CS7 Human Gastrula
Monkey Stage
11 dpf
12 dpf
13 dpf
14 dpf
16 dpf
17 dpf
C
UMAP_1
UMAP_2
Epiblast
Ectoderm
Primitive Streak
YS Mesoderm
HemoEndo Progen
Nascent Mesoderm
Advanced Mesoderm
Erythrocytes
Axial Mesoderm
Emergent Mesoderm
Endoderm
D
CS7 Human Ectoderm
SOX2
TFAP2A
ISL1
GATA3
UMAP_2
UMAP_1
Average Expression
E
CS7 Human Cell Types
YS Mesoderm
Primitive Streak
Nascent Mesoderm
Hemogenic Endothelial Progenitors
Erythrocytes
Epiblast
Endoderm
Emergent Mesoderm
Ectoderm
Axial Mesoderm
Advanced Mesoderm
Early Amnion
Early Gastrulating
Early PGC
ExE Mesenchyme
Late Amnion-1
Late Amnion-2
Late Gastrulating-1
Late Gastrulating-2
Postimplantation Early EPI
Postimplantation Late EPI
TE and derivatives
Visceral/Yolk Sac Endoderm
Allantois
Anterior PS
Blood Progenitors 1
Blood Progenitors 2
Caudal EPI
Caudal Mesoderm
Caudal Neurectoderm
Definitive Endoderm
Endothelium
EPI
Erythroid 1
Erythroid 2
Erythroid 3
ExE Ectoderm
ExE Endoderm
ExE Mesoderm
Gut
Haematoendothelial Progenitors
Intermediate Mesoderm
Mesenchyme
Mixed Mesoderm
Nascent Mesoderm
Notochord
Paraxial Mesoderm
Parietal Endoderm
PGC
Pharyngeal Mesoderm
PS
Rostral Neurectoderm
Somitic Mesoderm
Surface Ectoderm
Visceral Endoderm
Monkey Cell types (dpf 11–17)
Mouse Cell types (E6.5–7.5)
Average Predicted Score
Percent Cells with Predicted Score
F
Gastruloid Cell Types
ExE−like
hPGCLC
Endoderm
Mesoderm−2
Mesoderm−1
Ectoderm
EPI−like
Monkey Cell types (dpf 11–17)
Mouse Cell types (E6.5–7.5)
Average Predicted Score
Percent Cells with Predicted Score

Figure 3S. Supplemental information related to Figure 3

(A and B) Prediction score of mouse (A) and monkey (B) gastrula stages in CS7 human gastrula.

(C) UMAP projection showing 11 major cell types reported in CS7 human (Tyser et al., 2020).

(D) UMAP display of indicated markers expression in CS7 Ectoderm.

(E and F) Prediction score of E6.5–7.5 mouse and 11–17 dpf monkey gastrulating cell types in CS7 human gastrula (E) and gastruloids (F).

Figure 4S

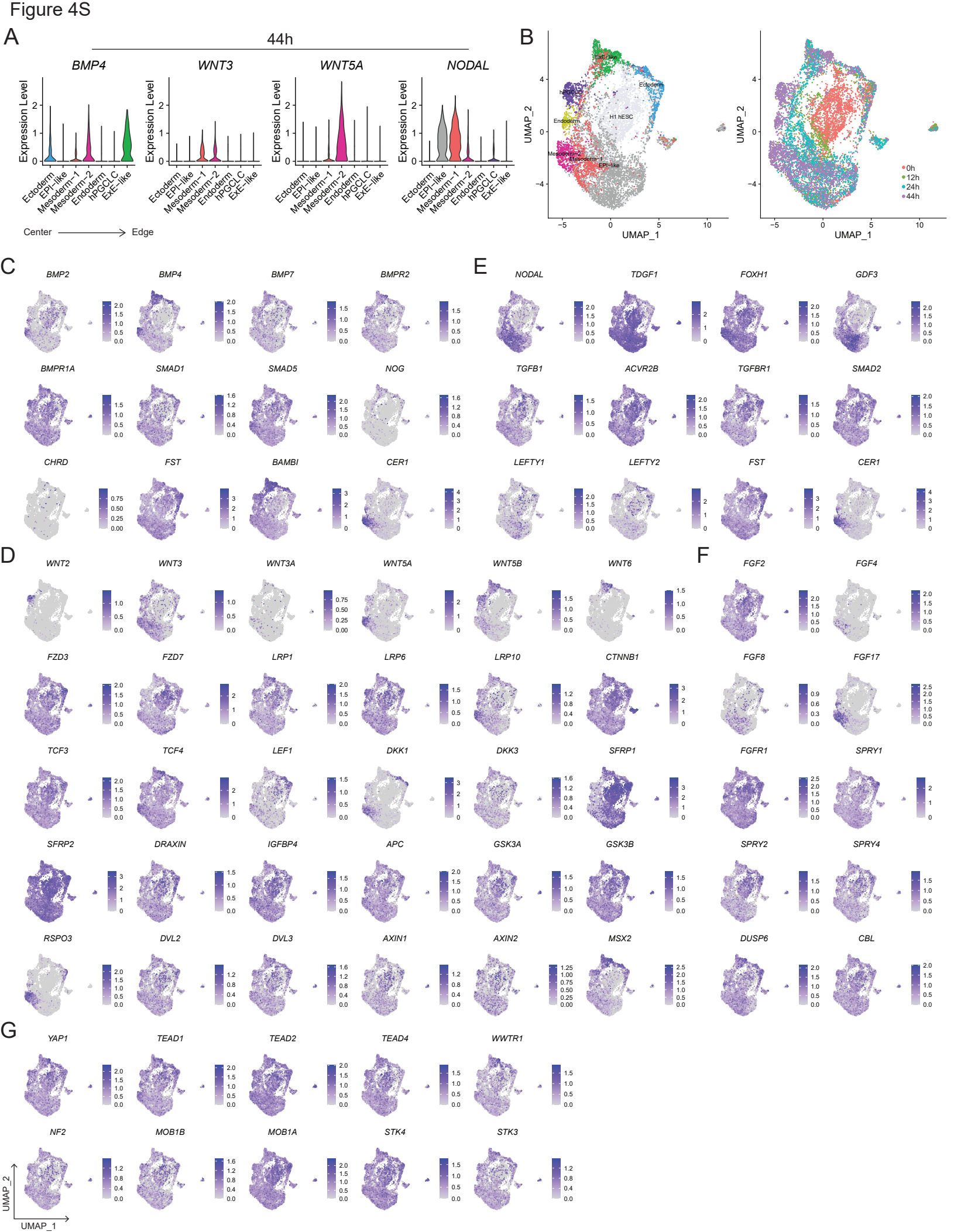
A
44h
BMP4
WNT3
WNT5A
NODAL
Expression Level
Ectoderm
EPI−like
Mesoderm−1
Mesoderm−2
Endoderm
hPGCLC
ExE−like
Center
Edge
B
UMAP_1
UMAP_2
0h
12h
24h
44h
C
BMP2
BMP4
BMP7
BMPR2
BMPR1A
SMAD1
SMAD5
NOG
CHRD
FST
BAMBI
CER1
D
WNT2
WNT3
WNT3A
WNT5A
WNT5B
WNT6
FZD3
FZD7
LRP1
LRP6
LRP10
CTNNB1
TCF3
TCF4
LEF1
DKK1
DKK3
SFRP1
SFRP2
DRAXIN
IGFBP4
APC
GSK3A
GSK3B
RSPO3
DVL2
DVL3
AXIN1
AXIN2
MSX2
E
NODAL
TDGF1
FOXH1
GDF3
TGFB1
ACVR2B
TGFBR1
SMAD2
LEFTY1
LEFTY2
FST
CER1
F
FGF2
FGF4
FGF8
FGF17
FGFR1
SPRY1
SPRY2
SPRY4
DUSP6
CBL
G
YAP1
TEAD1
TEAD2
TEAD4
WWTR1
NF2
MOB1B
MOB1A
STK4
STK3
UMAP_2
UMAP_1

Figure 4S. Supplement information related to Figure 4

(A) Expression of genes encoding indicated signaling molecules in 44h gastruloid.

(B) UMAP display of annotated gastruloid cell types at indicated time points.

(C–G) Gene expression of indicated components of BMP (B), NODAL (C), WNT (D), FGF (E), and HIPPO (F) signaling pathway in all cell types across all time points.

Figure 5S

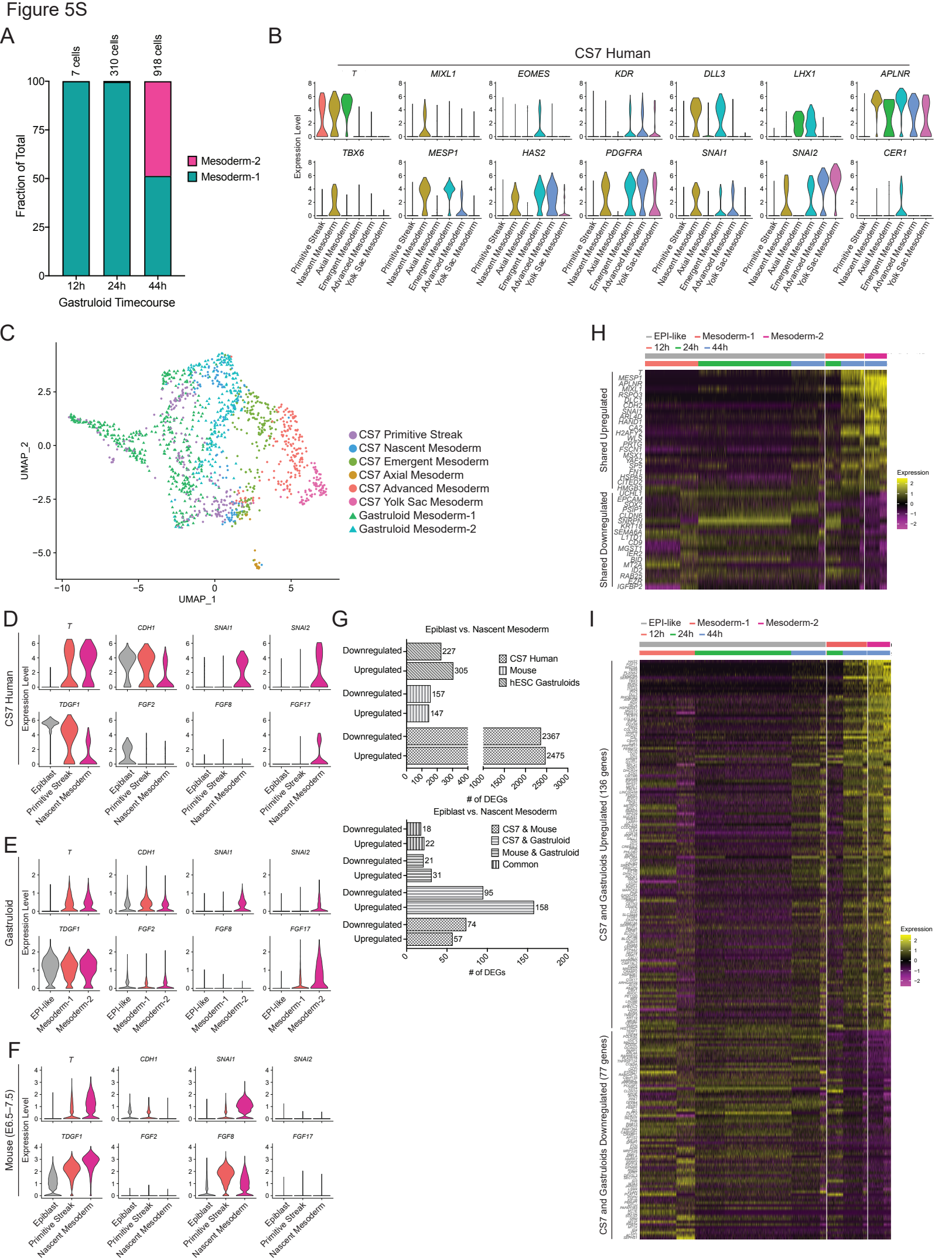
A
7 cells
310 cells
918 cells
Fraction of Total
Mesoderm-2
Mesoderm-1
12h
24h
44h
Gastruloid Timecourse
B
CS7 Human
T
MIXL1
EOMES
KDR
DLL3
LHX1
APLNR
TBX6
MESP1
HAS2
PDGFRA
SNAI1
SNAI2
CER1
Expression Level
Primitive Streak
Nascent Mesoderm
Axial Mesoderm
Emergent Mesoderm
Advanced Mesoderm
Yolk Sac Mesoderm
C
UMAP_1
UMAP_2
CS7 Primitive Streak
CS7 Nascent Mesoderm
CS7 Emergent Mesoderm
CS7 Axial Mesoderm
CS7 Advanced Mesoderm
CS7 Yolk Sac Mesoderm
Gastruloid Mesoderm-1
Gastruloid Mesoderm-2
D
CS7 Human
T
CDH1
SNAI1
SNAI2
TDGF1
FGF2
FGF8
FGF17
Expression Level
Epiblast
Primitive Streak
Nascent Mesoderm
E
Gastruloid
EPI-like
Mesoderm-1
Mesoderm-2
F
Mouse (E6.5–7.5)
G
Epiblast vs. Nascent Mesoderm
Downregulated
Upregulated
227
305
157
147
2367
2475
CS7 Human
Mouse
hESC Gastruloids
# of DEGs
CS7 & Mouse
CS7 & Gastruloid
Mouse & Gastruloid
Common
18
22
21
31
95
158
74
57
H
EPI-like
Mesoderm-1
Mesoderm-2
12h
24h
44h
Shared Upregulated
Shared Downregulated
Expression
I
CS7 and Gastruloids Upregulated (136 genes)
CS7 and Gastruloids Downregulated (77 genes)

Figure 5S. Supplement information related to Figure 5

(A) Fraction of gastruloid Mesoderm-1 and -2 cells at indicated time points.

(B) Expression of indicated PS and mesoderm markers in CS7 PS and mesoderm derivatives.

(C) UMAP projection of CS7 human primitive streak and mesoderm derivatives, and gastruloid Mesoderm-1 and -2 cells.

(D–F) Violin plots showing expression of indicated mesoderm markers in transition from EPI to nascent mesoderm cells in CS7 human gastrula (D), gastruloids (E), and mouse gastrula (F).

(G) Bar plots indicating number of downregulated and upregulated genes (top) and shared downregulated and upregulated genes (bottom) in Nascent Mesoderm (gastruloid Mesoderm-2 equivalent) compared to EPI (gastruloid EPI-like equivalent) in human, mouse, and hESC gastruloids.

(H) Heatmap depicting downregulated and upregulated genes of Nascent Mesoderm shared in human, mouse, and hESC gastruloids.

(I) Heatmap depicting downregulated and upregulated genes of Nascent Mesoderm shared in human, and hESC gastruloids but not in mouse.

Figure 6S

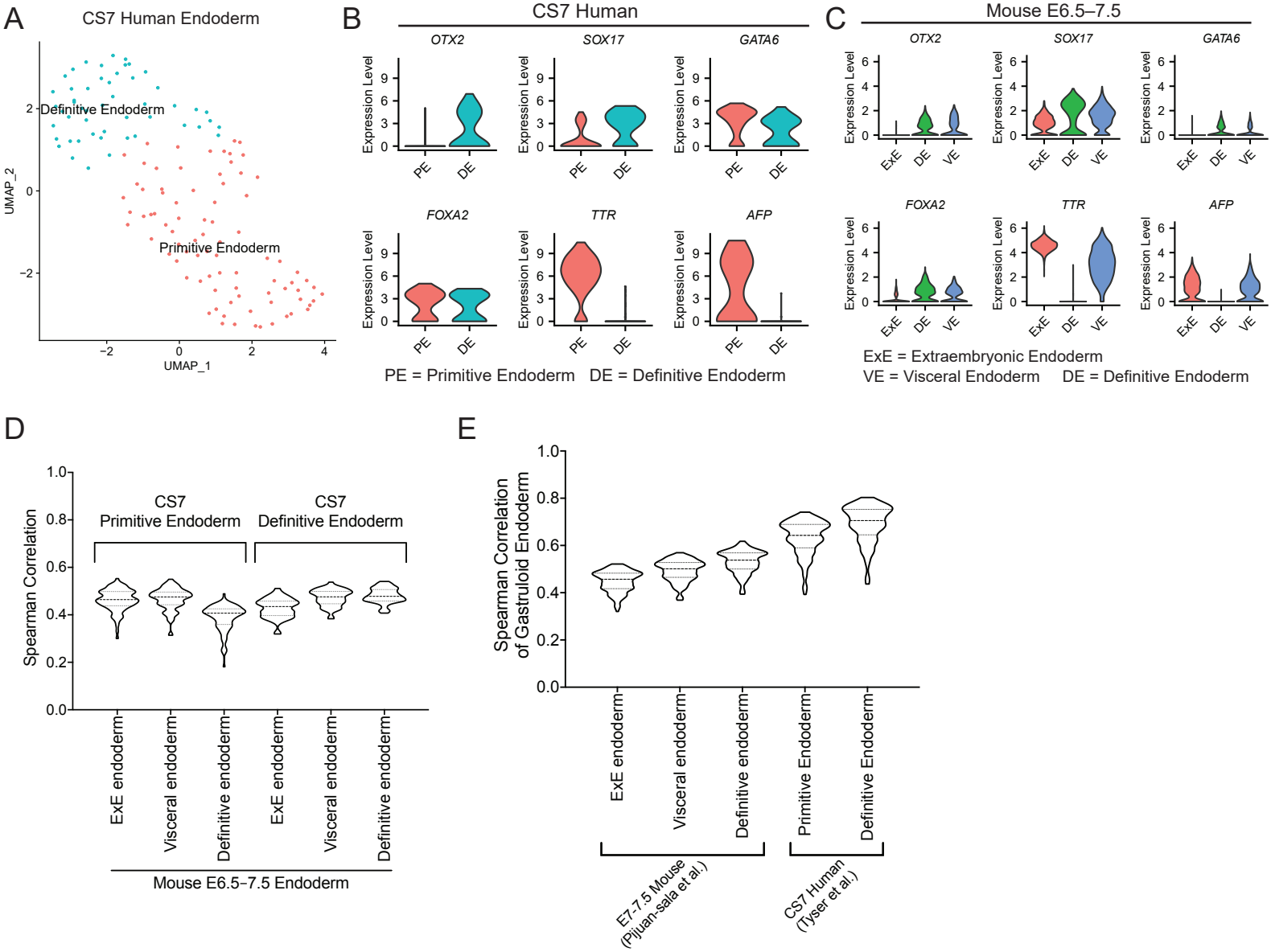
A
CS7 Human Endoderm
Definitive Endoderm
Primitive Endoderm
UMAP_1
UMAP_2
B
CS7 Human
OTX2
SOX17
GATA6
FOXA2
TTR
AFP
Expression Level
PE
DE
PE = Primitive Endoderm DE = Definitive Endoderm
C
Mouse E6.5–7.5
ExE
DE
VE
ExE = Extraembryonic Endoderm
VE = Visceral Endoderm DE = Definitive Endoderm
D
Spearman Correlation
CS7
Primitive Endoderm
CS7
Definitive Endoderm
ExE endoderm
Visceral endoderm
Definitive endoderm
Mouse E6.5–7.5 Endoderm
E
Spearman Correlation
of Gastruloid Endoderm
Primitive Endoderm
Definitive Endoderm
E7.5 Mouse
(Pijuan-sala et al.)
CS7 Human
(Tyser et al.)

Figure 6S. Supplemental information related to Figure 6

(A) UMAP projection of CS7 human Endoderm identifying PE and DE.

(B and C) Violin plots showing expression of indicated endoderm markers in human (B) and mouse (C).

(D) Average gene expression correlation of indicated human and mouse endoderm derivatives.

(E) Average gene expression correlation of gastruloid endoderm to indicated human and mouse endoderm derivatives.

Figure 7S

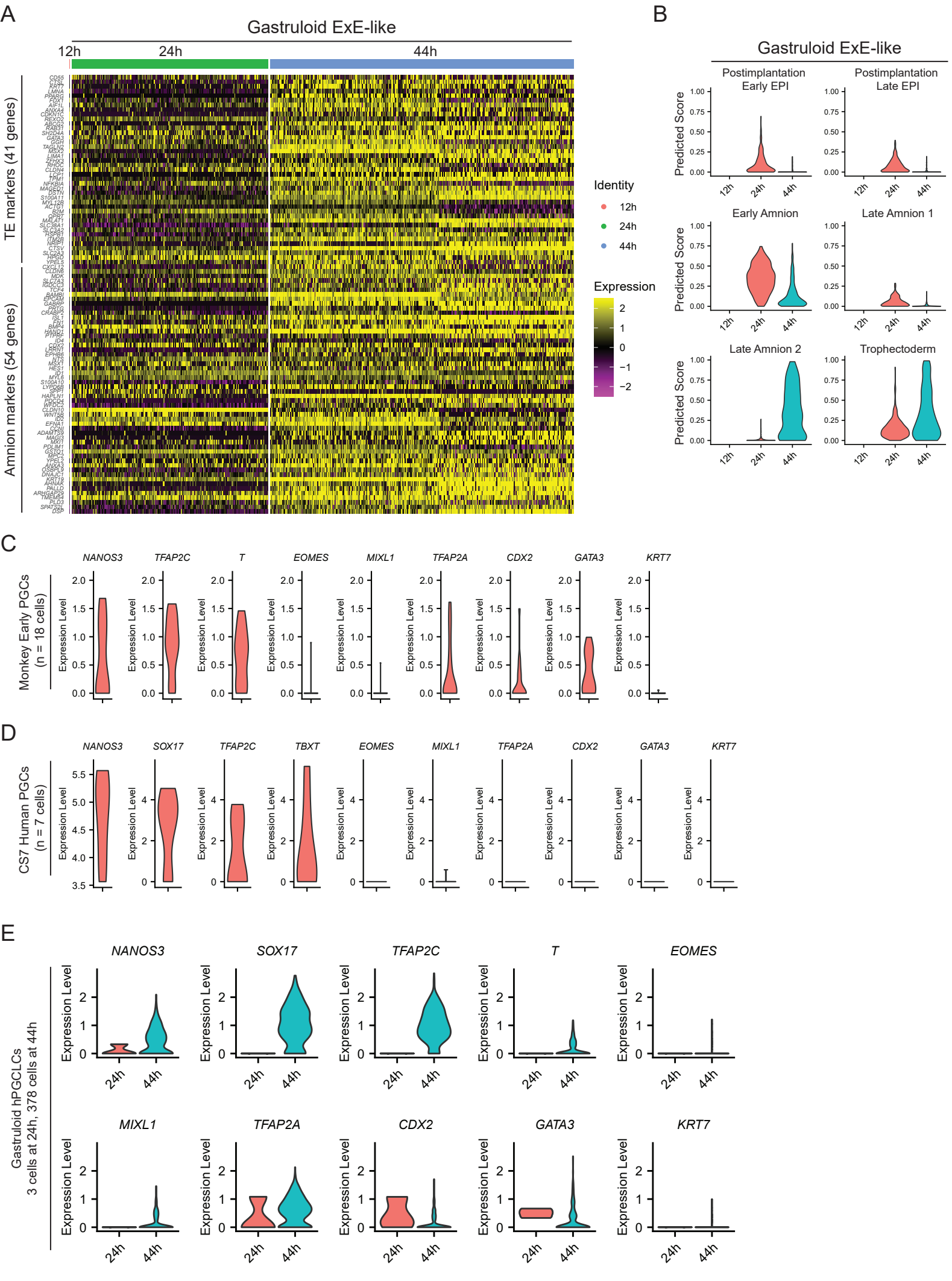
A
Gastruloid ExE-like
12h
24h
44h
TE markers (41 genes)
Amnion markers (54 genes)
Identity
12h
24h
44h
Expression
2
1
0
−1
−2
B
Gastruloid ExE-like
Postimplantation Early EPI
Postimplantation Late EPI
Early Amnion
Late Amnion 1
Late Amnion 2
Trophectoderm
Predicted Score
C
Monkey Early PGCs (n = 18 cells)
NANOS3
TFAP2C
T
EOMES
MIXL1
TFAP2A
CDX2
GATA3
KRT7
Expression Level
D
CS7 Human PGCs (n = 7 cells)
NANOS3
SOX17
TFAP2C
TBXT
EOMES
MIXL1
TFAP2A
CDX2
GATA3
KRT7
Expression Level
E
Gastruloid hPGCLCs
3 cells at 24h, 378 cells at 44h
NANOS3
SOX17
TFAP2C
T
EOMES
MIXL1
TFAP2A
CDX2
GATA3
KRT7
Expression Level
24h
44h

Figure 7S. Supplemental information related to Figure 7

(A) Heatmap showing expression of human and monkey TE markers in gastruloid ExE-like cells along the time course.

(B) Prediction score of monkey EPI, TE, and amnion in gastruloid ExE-like cells over the time course.

(C–E) Violin plot showing expression of indicated markers in monkey (C) and CS7 human (D) PGCs, and gastruloid hPGCLCs (E).